Supplementary Information

Photocurable bioresorbable adhesives as functional interfaces between flexible bioelectronic devices and soft biological tissues

Quansan Yang[1,2,3†], Tong Wei[4†], Rose T. Yin[5†], Mingzheng Wu[6†], Yameng Xu[7,8†], Jahyun Koo[9], Yeon Sik Choi[1,2,7], Zhaoqian Xie[10,11,12], Sheena W. Chen[13], Irawati Kandela[14,15], Shenglian Yao[16], Yujun Deng[3,17], Raudel Avila[3], Tzu-Li Liu[3], Wubin Bai[1,2,7,18], Yiyuan Yang[1,2,3], Mengdi Han[1,2], Qihui Zhang[7], Chad R. Haney[15,19,20], K. Benjamin Lee[13], Kedar Aras[5], Tong Wang[4], Min-Ho Seo[1,2,7,21], Haiwen Luan[1,2,3], Seung Min Lee[7], Anlil Brikha[15,19], Nayereh Ghoreishi-Haack[14], Lori Tran[14,15], Iwona Stepien[14,15], Fraser Aird[15], Emily A. Waters[15,19,20], Xinge Yu[22], Anthony Banks[1,2], Gregory D. Trachiotis[5,23], John M. Torkelson[4,7], Yonggang Huang[1,3,7,24], Yevgenia Kozorovitskiy[6,15*], Igor R. Efimov[5*], John A. Rogers[1,2,3,7,20,25*]

[1]Center for Bio-Integrated Electronics, Northwestern University, Evanston, IL 60208, USA. [2]Querrey Simpson Institute for Biotechnology, Northwestern University, Evanston, IL 60208, USA. [3]Department of Mechanical Engineering, Northwestern University, Evanston, IL 60208, USA. [4]Department of Chemical and Biological Engineering, Northwestern University, Evanston, IL 60208, USA. [5]Department of Biomedical Engineering, The George Washington University, Washington, DC, 20052, USA. [6]Department of Neurobiology, Northwestern University, Evanston, IL 60208, USA. [7]Department of Materials Science and Engineering, Northwestern University, Evanston, IL 60208, USA. [8]Institute of Materials Science and Engineering, Washington University in St. Louis, St. Louis, MO 63130, USA. [9]School of Biomedical Engineering, Korea University, Seoul 02841, Republic of Korea. [10]State Key Laboratory of Structural Analysis for Industrial Equipment, Dalian University of Technology, Dalian 116024, China. [11]Department of Engineering Mechanics, Dalian University of Technology, Dalian 116024, China. [12]Ningbo Institute of Dalian University of Technology, Ningbo, 315016, China. [13]Department of Surgery, The George Washington University, Washington, DC 20052, USA. [14]Developmental Therapeutics Core, Northwestern University, Evanston, IL 60208, USA. [15]Chemistry Life Processes Institute, Northwestern University, Evanston, IL 60208, USA. [16]School of Materials Science and Engineering, University of Science & Technology Beijing, Beijing 100083, China. [17]State Key Laboratory of Mechanical System and Vibration, Shanghai Jiao Tong University, Shanghai 200240, China.[18]Department of Applied Physical Sciences, University of North Carolina at Chapel Hill, NC 27599, USA. [19]Center for Advanced Molecular Imaging, Northwestern University, Evanston, IL 60208, USA. [20]Department of Biomedical Engineering, Northwestern University, Evanston, IL 60208, USA. [21]School of Biomedical Convergence Engineering, College of Information & Biomedical Engineering, Pusan National University, Pusan 43241, Republic of Korea. [22]Department of Biomedical Engineering, City University of Hong Kong, Hong Kong 999077, China. [23]DC Veterans Affairs Medical Center, The George Washington University, Washington, DC 20052, USA. [24]Departments of Civil and Environmental Engineering, Northwestern University, Evanston, IL 60208, USA. [25]Department of Neurological Surgery, Feinberg School of Medicine, Northwestern University, Chicago, IL 60611, USA. † These authors contributed equally to this work. * To whom correspondence should be addressed to yevgenia.kozorovitskiy@northwestern.edu (Y.K.), efimov@gwu.edu (I.R.E.), and jrogers@northwestern.edu (J.A.R.).

Supplementary Notes

Supplementary Note 1. Comparison with existing adhesive materials

Commercially available adhesives for bioelectronics are far from ideal. Various options, listed in Supplementary Table 1, include natural/biological adhesives and synthetic adhesives. As an example of a natural/biological adhesive, Tisseel (fibrin glue; Baxter) has low matrix toughness (< 20 J/m^2) and low adhesion[1]. As an example of a synthetic adhesive, cyanoacrylate-based adhesive is cytotoxic to some degree[2] and rigid and brittle, and it is not compatible with wet tissue surfaces[3,4]. Almost all the commercial adhesives are non-conductive, and therefore are not compatible with many types of bioelectronics devices. These commercially available adhesives fail to address key demands for the use of advanced implantable systems.

We experimentally compared our material to commercially available tissue adhesives. The main areas of focus are inabilities to support (1) reliable adhesion to wet surfaces and (2) function as electrical interfaces. To illustrate the deficiencies in the first area, we attempted to use certain of these adhesives (n-butyl Cyanoacrylate adhesive; Vetbond tissue adhesive; 3M, MN, USA) to bond a flexible multi-sensing array (Supplementary Fig. 31a) onto a piece of porcine skin. These liquid-type tissue adhesives were spread carefully on the porcine skin (Supplementary Fig. 31b). The device was then placed directly on top (Supplementary Fig. 31c) with mild pressure for 10 s (Supplementary Fig. 31d). After curing for 5 min, we observed poor adhesion, such that the device was easily delaminated from the skin (Supplementary Fig. 31e-h). As such, this adhesive is not suitable for wet tissues, and as such it fails to act as a suitable bioelectronics interface material. As a comment on deficiencies in the second area, we note that most commercial tissue adhesives are

inappropriate as electrical interfaces. To illustrate this issue, we characterized the electrical performance of flexible multielectrode array (MEA) before and after applying two representative natural/biological and synthetic tissue adhesives (natural adhesive, FloSeal, Baxter, IL, USA; synthetic adhesive, Dermabond, Ethicon Inc., NJ, USA). The MEA (parylene/Cr/Au/parylene: 4 μm/30 nm/300 nm/4 μm) has electrodes with the dimensions of 500 μm × 500 μm and the spacing between two adjacent electrodes is 1 mm. A digital potentiostat (Metrohm Autolab, Utrecht, Netherlands) with an Ag-AgCl reference electrode recorded the impedance spectrum between two adjacent electrodes at room temperature with 0.1 M PBS before (Supplementary Fig. 31i) and after (Supplementary Fig. 31j) application of these commercial adhesives. The impedance spectra of the adjacent electrodes before (black for FloSeal and grey for Dermabond) and after (red for FloSeal and orange for Dermabond) application of adhesives appear in Supplementary Fig. 31k, indicating that the impedance increases by three orders of magnitude in both cases due to the dielectric, non-conductive nature of these materials. We conclude, therefore, that these commercial adhesives cannot be applied as bioelectronic interface materials to soft biological tissues and that they fail to satisfy the essential requirements for such applications.

Supplementary Table 2 lists the main disadvantages associated with published reports on tissue adhesives[5–7] and their inability to address the device demonstrations described in our manuscript. Reported liquid-type adhesives[5] provide lower toughness and adhesion compared with the BTIM. Patch-type adhesives, such as PAM-Alg patches[7] and double-sided tapes[6], possess similar matrix toughness and interfacial adhesive energy to BTIM, which have potential for reliable and robust adhesion on wet surfaces. However, these adhesives (1) require compression to enable bonding and (2) cannot be applied easily to highly structured or curved surfaces. The first issue can be problematic for use with fragile bioelectronic devices. For instance, the flexible multielectrode

array (MEA) example in our manuscript is unchanged by application of the BTIM, as demonstrated by benchtop characterization results (Fig. 2l-m, Supplementary Fig. 17-18) and by animal trials (Fig. 6). Supplementary Fig. 32a presents the photograph of the MEA device (parylene/Cr/Au/parylene: 4 μm/30 nm/300 nm/4 μm). We observe that pressure (pressure: 20 kPa; duration: 1 min; Supplementary Fig. 32b) applied to bond the MEA to biological tissue with the compression-assisted adhesive patch leads to changes in performance. Measurements to quantify these effects use previous protocols[8–11], where a digital potentiostat (Metrohm Autolab, Utrecht, Netherlands) with an Ag-AgCl reference electrode and a Pt counter electrode capture the impedance spectrum of these MEA electrodes in 0.1 M PBS at room temperature. Representative impedance spectra of an MEA electrode before (blue) and after (red) compression appear in Supplementary Fig. 32c, showing that the impedance increases by two orders of magnitude due to compression induced fracture of certain of the electrodes and interconnects. A statistical representation of these results appears in Supplementary Fig. 32d, indicating that 2 out of 6 electrodes fracture during the compression, where the impedance increases from 8.0 kΩ and 7.5 kΩ to 193.7 kΩ and 154.7 kΩ, respectively, at 1 kHz in 0.1 M PBS at room temperature (number of measured electrodes: 6; impedance before compression: 8.0 kΩ, 7.5 kΩ, 8.9 kΩ, 8.0 kΩ, 7.1 kΩ, and 7.8 kΩ, respectively; corresponding impedance after compression: 193.7 kΩ, 154.7 kΩ, 14.1 kΩ, 8.1 kΩ, 7.3 kΩ, and 7.9 kΩ).

The second issue is that patch-type adhesives fail to provide conformally adhered interfaces for bioelectronic devices with highly structured or curved surfaces due to the fixed shape of these materials before application. Because the BTIM can be applied as a liquid, it is compatible even with 3D curved electronics (Extended Data Fig. 1 and Supplementary Fig. 3).

Supplementary Note 2. Chemical characterization procedures and results

We utilized matrix-assisted laser desorption/ionization-time of light mass spectrometry (MALDI-ToF) and ^{1}H NMR spectroscopy to prove the existence of lactide acid units and acrylate groups on the end of the macromers. Since NMR characterization of high molecular weight PEG (35,000 g/mol) is dominated by protons from PEG, leading to an indetectable chain end signal, we used a small molecular weight PEG (3,350 g/mol) as the model system for these studies, with the same chemical synthesis procedures as described in our manuscript. Supplementary Fig. 1b shows the ^{1}H NMR results for lactide acid units and acrylate groups. Peak d and e indicate the existence of the lactide acid units, and peak a, b, and c indicate the existence of the acrylate groups in the PEG-4LA-DA macromer (MW: ~ 3,350 g/mol). All the results prove that the lactide acid units and acrylate groups are successfully connected to the macromers. Supplementary Fig. 1c-d present the MALDI-ToF MS results for PEG (a; MW: ~ 3,350 g/mol) and for PEG-2LA (b). The PEG-2LA has ~1.5 lactide acid units on average on each chain end. The results suggest that the lactide acid units are successfully connected to the ends of PEG macromers.

Supplementary Note 3. APTES surface functionalization

The APTES layer is stable in air and water for at least two weeks (Extended Data Fig. 2e). We measured the thickness of the APTES layer on a silicon wafer via ellipsometry (M-2000D; J.A. Woollam Co., Inc, NE, USA), using procedures similar to those described elsewhere[12]. Measurements were performed at wavelengths from 400 to 1000 nm (with an incident angle of 65°). Data were fitted to a Cauchy model composed of a silicon substrate with a 1.3-nm-thick native SiO_2 layer and a layer of APTES on top. Three pieces of wafer treated with APTES were exposed to air and submerged in water for 20 days, respectively, for the study of layer stability. Immediately after the APTES treatment, the thickness of the APTES layer was ~ 1.4 – 1.5 nm. By contrast, the cleaned, untreated silicon wafer exhibits an APTES layer with a thickness of 0 nm, measured by the same setup. As shown in Extended Data Fig. 2e, the thickness of the APTES layer exposed in the air is 1.50 ± 0.06 nm, 1.53 ± 0.05 nm, 1.48 ± 0.04 nm, 1.52 ± 0.04 nm, 1.48 ± 0.04 nm, 1.52 ± 0.08 nm, and 1.57 ± 0.05 nm on day 0, 2, 4, 6, 12, 14, and 20, respectively, and remained invariant for 20 days, to within experimental uncertainties. The thickness of the APTES layer in water also remained constant within experimental uncertainties. The thickness of the APTES layer submerged in water was 1.43 ± 0.05 nm, 1.27 ± 0.05 nm, 1.37 ± 0.08 nm, 1.33 ± 0.08 nm, 1.32 ± 0.08 nm, 1.35 ± 0.05 nm, and 1.28 ± 0.08 nm on day 0, 2, 4, 6, 12, 14, and 20, respectively. These results indicate that our functionalization protocol produces a layer of APTES that is stable in water and air for at least 20 days.

After APTES treatment and the BTIM encapsulation, the schematic illustration and photograph of the BTIM-encapsulated MEA device appear in Supplementary Fig. 17c-d (BTIM thickness: ~ 500 μm). Representative impedance spectra of an MEA electrode before (blue) and after (red) BTIM application indicate negligible differences (Supplementary Fig. 17e-g). Statistical results for

impedance values before and after BTIM application are 8.2 ± 0.3 kΩ and 7.9 ± 0.4 kΩ, respectively, at 1 kHz in 0.1 M PBS at room temperature. The results reveal that the APTES treatment and the BTIM encapsulation have an insignificant impact on electrode functionality

Supplementary Note 4. Effects of the ionic crosslinking density and the amount of lactide repeat units on BTIM mechanical properties

The ionic crosslinking density and the amount of lactide repeat units on each end of the PEG influence the elongation and fracture energy (Supplementary Fig. 5). For concentrations of ionic crosslinker (Supplementary Fig. 5c), where the concentration of Ca^{2+} is 12.5, 15, 20, or 20 mM, the elongation values are around 10, 11, 11, and 8, respectively. The corresponding fracture energy values are around 1600, 1900, 1600, and 900 J/m^2, respectively. The highest fracture energy (1900 J/m^2) occurs at an intermediate concentration of Ca^{2+} (15 mM). The fracture energy decreases as the Ca^{2+} concentration increases from 15 to 25 mM, largely due to the more highly crosslinked, but smaller deformed zone around the root of the notch to break the alginate chains[13]. For the amount of lactide repeat units on each end of the PEG (amount x = 0, 2, 4 and 10; Supplementary Fig. 5d), the elongation values are around 11, 10, 5, and 4, respectively (in this case Ca^{2+} concentration: 15 mM). The corresponding fracture energy values are around 1900, 1800, 800, and 800 J/m^2, respectively. The results indicate a reduction in elongation and fracture energy with an increase of lactide repeat units, likely as a result of the rigidity associated with the ester groups[14].

Supplementary Note 5. Spatially confined coatings with uniform thickness

The BTIM can yield spatially confined coatings with uniform thicknesses, as quantified by *in vivo* and *ex vivo* studies. The studies involved devices with integrated bioresorbable frames to restrict the flow, as in Supplementary Fig. 25d, or with removable biocompatible frames, as in Supplementary Fig. 33. In the former case, the frames were fabricated together with the devices or they were simply bonded after separate fabrication. Supplementary Fig. 25d shows a biodegradable PLGA frame (5 mm × 5 mm × ~ 200 μm), connected to a pair of electrodes of a wireless cardiac pacemaker during fabrication. This frame enabled spatially confined delivery of adhesive on a moving chicken heart *ex vivo*. Removeable, biocompatible frames were placed onto tissue surfaces before applying the BTIM and removed after fully curing the BTIM. Supplementary Fig. 33 shows the case of a PDMS frame of this type (thickness: 500 μm) for use with dorsal-subcutaneous wireless optoelectronic devices. The results in Fig. 4k-l show that the BTIM layer is uniform in thickness, with a flat and smooth top surface, enabled by the initial honey-like viscosity. One representative example is the BTIM adhesive conduit for electronic interconnects/cables. Here, the spatial confinement was achieved with a PDMS frame. After UV curing, the BTIM adhesive conduit presents a flat and smooth top surface. The thickness of the BTIM layer can be calculated geometrically, according to

$$Thickness_{desired} = Volume_{applied}/Spreading\ area_{designed}$$

Supplementary Note 6. Integration with device arrays and 3D multilayer, electrode-embedded, and electrode-exposed electronic systems

A variety of device geometries and tissues can be addressed using the schemes of Fig. 1b-d, as shown in Extended Data Fig. 1 and Supplementary Fig. 2-3. As an example, the encapsulation strategy (adhesive thickness: 500 μm) can anchor multiple components (silicon chips coated with a layer of fluorescent acrylic paint; size: 4 mm × 4 mm × 500 μm; number: 19) onto a piece of porcine skin in the shape of 'NU', in a manner that is robust to bending and twisting (Supplementary Fig. 2a-d). Repeating the encapsulation strategy can yield multilayered systems, as in the three-layer example of Supplementary Fig. 2e-f.

The BTIM can also serve as a supporting matrix for fragile three-dimensional (3D) bioelectronic systems. Demonstrations include electrode-embedded (Extended Data Fig. 1 and electrode-exposed (Supplementary Fig. 3) electronic structures. The bioadhesive matrix allows manual manipulation without damaging fragile features, and with the ability to bond to moving, curved tissue surfaces. The measured electrode is in the central area of the 3D structure shown in Extended Data Fig. 1d. Impedance measurements over frequencies between 10^2 to 10^5 Hz utilize a commercial potentiometer (Autolab PGSTAT128N; Metrohm AG, Herisau, Switzerland) with an Ag/AgCl reference in PBS (pH 7.4) at room temperature. For the examples here, without the matrix, pressure as low as 5 kPa plastically deforms and fractures materials in these 3D bioelectronics. Impedance measurements demonstrate that the magnitude and phase angle change by 97.6 % and 49.1° at 1 kHz, respectively. When embedded in the bioadhesive matrix, the same structures under similar pressures (0 – 5 kPa) undergo minimal changes of impedance and phase angle (36.7 % and 0.1° at 1 kHz, respectively), with negligible deformations (Extended Data Fig. 1h-i). The results

under dynamic compression fatigue tests (pressure: 2 kPa; cycle number: 10^4) reveal minimal changes as well (6.8% and 0.4° at 1 kHz, respectively; Extended Data Fig. 1j-k). For the electrode-exposed devices, capillary interactions lead to the filling of the bioadhesive into the interior spaces of the 3D architectures, as shown in the complex curvilinear examples in Supplementary Fig. 3. The inset highlights this type of device that includes an operating μ-ILED.

Supplementary Note 7. Measurement procedures and results on bioresorbability

The BTIM can disintegrate *in vivo* through biodegradation of the PEG-LA-DA network and the chitosan, and through the dissolution of the alginate network. This dissolution process follows from the release of the divalent ions that cross-link the alginate network into the surrounding media due to exchange reactions with monovalent cations such as sodium ions[15]. The mammals lack enzymes (i.e., alginase) to cleave the alginate chains. Previous reports[16] indicate that after the dissolution of the alginate network in mammals, the alginate component goes into circulation within 24 hours. The fraction with a small molecular weight (i.e., $\leq$ 48,000 g/mol) likely enters the terminal lymphatic vessels, ultimately excreted in the urine after passage through the kidneys within 24 hours. The fraction with a higher molecular weight remains in circulation and does not readily accumulate in any of the organs. The molecular weight distribution of the alginate used in this study is relatively broad (~ 25,000 – 125,000 g/mol). Utilizing alginate with a molecular weight lower than ~ 48,000 g/mol increases the rate of blood clearance via excretion through the kidneys.

Supplementary Note 8. Cytocompatibility and biocompatibility

(1) *In vitro* cytocompatibility

A mouse cell line (ATCC® CCL-1™, L-929; VA, USA) was used for live/dead cell viability assays and cell migration characterizations. Live/dead cell assays on cured and uncured BTIM indicate negligible cytotoxicity. Here, L929 cells were seeded in 24-well plates. After the formation of a monolayer, the BTIM and uncured precursors were introduced on the top of these cells and kept for 5 days. The viability tests in Supplementary Fig. 14d show that the percentages of the live cells for cases of cell culture media (control group), cured BTIM (5-mm-diameter; thickness: ~ 0.5 mm), and uncured BTIM precursors (5 wt % in cell culture media) are 97.4 ± 0.7, 95.6 ± 1.3, and 94.9 ± 1.0, respectively. We note that the uncured precursors used here have a much higher weight percentage in cell culture media (5 wt %) compared with that in animal models (e.g., 50 μL uncured precursors in a mouse model with a weight of 20 g for dorsal subcutaneous optoelectronics; weight percentage: 0.25 wt %). Studies of cell migration into pieces of the BTIM that are immersed in the cell culture medium also determine the *in vitro* cytocompatibility. Confocal imaging of the BTIM after soaking for one week reveals that live cells exist in the BTIM (Supplementary Fig. 14e-f). Cells adhere to the polymer matrix in the BTIM through SEM imaging (Supplementary Fig. 14g). All results above indicate that the BTIM is compatible with cells *in vitro*.

(2) *In vivo* biocompatibility

Studies of the effect of the BTIM, including the UV exposure, on wound healing behaviors of skin in mouse models, demonstrate its *in vivo* biocompatibility. The experiment involves three groups:

single UV exposure, BTIM that includes UV exposure, and Vetbond glue (3M, MN, USA). For the group with single UV exposure, direct exposing UV on the dorsal skin of rats finalizes the process (Supplementary Fig. 15). For the groups with the BTIM and Vetbond glue, BTIM or Vetbond glue seals a surgical site wound in the dorsal skin (length: ~ 15 mm), as shown in Supplementary Fig. 15b-c. Supplementary Fig. 15d-e present the healing behaviors of the wound with the BTIM and Vetbond glue on day 5 post-surgery, respectively. The wound sealed with the BTIM heals closely; however, the open cut remains on the skin that is sealed with Vetbond glue. Supplementary Fig. 15f tracks the body weights of mice in all groups within 2 weeks post-surgery, suggesting the weight of all mice stabilizes in the first 2 days post-surgery, with appropriate gain in subsequent days. After 2 weeks post-surgery, histological evaluations of skin tissues by a double-blinded, clinical-scoring system on a scale of 0 to 5 determine the level of inflammation and fibrosis in each group, as shown in Supplementary Fig. 15g. The scoring system is scaled as follows: none (0), mild (1), moderate (2), severe (3), and very severe (4). The average scores of inflammation in the control group and experimental groups with single UV exposure, BTIM that includes UV exposure, and Vetbond glue are 0, 0, 0.3, 0, respectively. The corresponding scores in fibrosis are 0.8, 1.2, 1.0, and 1.0, respectively. Altogether, the results above support the biocompatibility of the BTIM, associated with faster and better wound healing process compared with conventional tissue glue.

Supplementary Note 9. Measurement of device translation

Device displacement between time points corresponds to the magnitude of the displacement vector between the device centroids, i.e. $\sqrt{(x_2 - x_1)^2 + (y_2 - y_1)^2 + (z_2 - z_1)^2}$, where (x_1, y_1, z_1) and (x_2, y_2, z_2) represent device centroids at timepoints 1 and 2. The measurements rely on the centroid position of the devices measured for the first time as a reference. Relative to this reference, the centroid positions of devices on the following days are calculated.

For dorsal subcutaneous wireless devices for phototherapy, the overall translational movements are 1.6 ± 1.2 mm from day 2 to day 5 and 0.8 ± 0.6 mm from day 5 to day 8 post-surgery (Fig. 3e) for the encapsulation strategy. In the interface method, the values are 2.9 and 3.0 mm, respectively (Supplementary Fig. 19b). By contrast, the device mounted in the same locations but covered with a non-adhesive hydrogel shows motions of 5.9 mm and 16.9 mm, respectively (Fig. 3e).

For the wireless devices that are placed above the exposed brain without insertion for transcranial optogenetic stimulation, the configuration facilitates monitoring of the position of the μ-ILED (270 μm × 220 μm × 50 μm) at the end of the probe. Extended Data Fig. 5a presents photographs of the BTIM-encapsulated and non-adhesive devices during surgery. The positions of BTIM-encapsulated devices (first row) and non-adhesive (second row) devices on day 1 (white), 4 (blue), and 7 (purple) post-surgery determined by MicroCT appear on the rest part of Extended Data Fig. 5a. The BTIM-encapsulated device remains in its original location throughout the period of study, to within experimental uncertainties. By contrast, the non-adhesive device shows significant translation and rotation under otherwise identical conditions. The stabilization of the μ-ILED provided by the BTIM dramatically increases the rate of success of transcranial optogenetic experiments. Statistical analyses in Extended Data Fig. 5b-c summarize the net translation and rotation of the μ-ILED in the BTIM-encapsulated (blue) and non-adhesive (red) devices on day 4

and 7 compared with those on day 1 post-surgery. The results reveal that the displacements of the μ-ILED in the BTIM-encapsulated devices are less than 70 μm within one week. By contrast, the displacements in the non-adhesive devices are ~ 600 μm from day 1 to day 4 and ~ 470 μm from day 4 to day 7. The translations of μ-ILED in non-adhesive devices are larger than the dimensions of the μ-ILED (270 μm × 220 μm × 50 μm), suggesting that the regions of optically stimulated tissue also change significantly. For rotation, the μLED in the non-adhesive case presents a rotation of ~ 3.2º from day 1 to day 4 and ~ 2.0º from day 4 to day 7. By contrast, the μ-ILED with the BTIM rotates less than 0.7º in this period of study. The BTIM-encapsulated device remains on the skull day 50 post-surgery, as determined by MicroCT, shown in Fig. 4d. By contrast, the non-adhesive device detaches from the skull and fails to provide optical stimulation.

Supplementary Note 10. External subdermal ECG acquisition system

To demonstrate the functionality of BTIM-encapsulated wireless cardiac pacemakers, we used an external acquisition system (PowerLab) to record ECG signals, as shown in Supplementary Fig. 27. Three subdermal ECG needle electrodes are placed on the rat in the Lead I position (positive electrode on right arm, negative electrode on left arm, and ground electrode on the led), as shown in Supplementary Fig. 27a. The PowerLab acquisition hardware directly filters the signal using a Mains filter and a low pass 2 kHz filter. The filtered ECG signals appear in the LabChart signal analysis software on a workstation computer (Supplementary Fig. 27b-d). The subdermal electrodes are manually attached for each recording session. The ECG signal morphology can vary depending on the position of the heart relative to the electrode location. Due to small, uncontrolled variations, the electrodes may be placed in slightly different locations relative to the anatomy of the rat. As a consequence, some subtle differences in the resultant ECG signals may result, but these differences do not affect the visualization of the capture of the heart by the BITM-integrated wireless pacemaker.

Supplementary Note 11. Failure modes and potential solutions to material reliability for long-term diagnosis and treatment of implantable electronics

The failure modes include (1) mechanical/physical degradation, (2) chemical/electrical leakage, and (3) compromised interfaces and immune reactions.

Failure mode 1 – mechanical/physical degradation Implantable bioelectronics devices must operate in the presence of cyclic deformations associated with the natural movement of tissues. Resulting mechanical fatigue can lead to plastic deformation and consequent structural damage and growth of cracks in the encapsulating materials and/or the sensing/actuating elements[17]. Fatigue of the electronics also weakens the device architecture in ways that can lead to delamination of these layers. All such phenomena reduce the device lifetime.

Failure mode 2 – chemical/electrical leakage Encapsulating materials are critical to long-term stability because electronic materials and the electrical currents supported by them are sensitive to water and water vapor, as well as other aspects of the chemical environment. Recent studies suggest that inorganic materials, such as monocrystalline silicon[18], thermally-grown silicon dioxide[19], and silicon carbide[18] offer superior characteristics as biofluid barriers. The mechanical fragility and complex fabrication steps associated with these materials represent disadvantages. Mechanically robust organic materials present some promise, such as parylene, but these polymers and other alternatives have water vapor transmission rates that are far higher than those of inorganic materials.

Failure mode 3 – compromised interfaces and immune reactions The interface failures include (1) insufficient adhesion to tissues and (2) mechanical and chemical changes induced by the formation of fibrotic capsules. Weak adhesion can lead to loss of physical contact, and associated decreases

in measurement accuracy, reductions in treatment efficiency and uncontrolled movements of the devices. The formation of fibrotic capsules is a common challenge for nearly all types of medical implants. Severe fibrosis can disrupt electrical connections to tissues and it can block light transmission to and from points of interest. Potential solutions For long-term operation, the device materials must address the failure modes outlined above. (1) The device materials should be compliant to dynamic deformations and movements of biological tissues, without mechanical fatigue, fracture or loss of adhesion. Intrinsically stretchable organic materials or serpentine-type structures in inorganic materials are preferred for these reasons. (2) The outer layer of the devices should serve as a barrier to biofluid penetration. Polymer coatings (polyimide, parylene, and epoxy), inorganic layers (mono-Si, SiN_x, SiO_2, and Al_2O_3), and multilayer structures (ZrO_2/Al_2O_3) can be valuable for such purposes[16]. These materials must be compatible with diverse, complex physiological conditions, where key parameters are pH, ionic content, temperature, and enzyme concentrations. (3) The adhesion to the tissue should remain robust to ensure positional stability and functional interfaces. The formation of fibrotic capsules is a challenge for nearly all types of medical implants. Thin, mechanically compliant implants suppress fibrotic responses and other foreign body reactions[20,21]. Doping of anti-inflammatory drugs, such as dexamethasone[20,21], into the device materials may further reduce inflammatory reactions. The combined use of mechanical and pharmacological approaches offers some promise in minimizing the formation of fibrotic capsules.

Supplementary Table

Supplementary Table 1 | Comparisons of the BTIM system with commercially available tissue adhesives.

	Representative nature/biological adhesives				Representative synthetic adhesives		Our BTIM
	Tisseel	**TachoSil**	**FloSeal**	**GRF**	**Dermabond**	**CoSeal**	
Main constituent	Fibrin	Fibrin	Collagen	Gelatin	Cyanoacrylate	Poly (ethylene glycol)	PEG-LA-DA/Alg
Application mode	Spary/speading	Compression	Spreading	Spreading	Spreading	Spary/spreading	Spreading
Modulus	< 100 kPa	> 100 MPa	< 100 kPa	< 100 kPa	> 100 MPa	< 100 kPa	~ 30 kPa
Optical transparency	Transparent	Opaque	Opaque	Opaque	Transparent	Transparent	Transparent
Electrical conductivity	None	None	None	None	None	None	Similar to biofluids
Other challenges	• Low matrix toughness • Low adhesion • Incompatibility with wet surfaces	• Low adhesion • Incompatibility with wet surfaces	• Long time required to form bonds	• Heating required	• Rigidity • Cytotoxicity • Incompatibility with wet surfaces	• Low matrix toughness • Low adhesion	\

Supplementary Tale 2 | Comparisons of the BTIM system with previously reported tissue adhesives, in the context of applications as bioelectronic interface materials to soft biological tissues.

Types of advanced bioelectronics/ optoelectronics	PAM-Alg patchs[7]	Double-sided tapes[6]	Printable HAPE-Py hydrogels[5]	Our BTIM
Main challenges as bioelectronic interface materials	• Lack of adhesion mechanism to devices • Compression required (Supplementary Fig. 32) • Lack of bioresorbability • Incompatibility with highly structured and curved surfaces • Lack of selective adhesion • Can only be used as encapsulation coatings	• Compression required (Supplementary Fig. 32) • Incompatibility with highly structured and curved surfaces • Can only be used as interface layers	• Low matrix toughness and interfacial adhesion • Lack of transparency • Lack of bioresorbability • Lack of selective adhesion	\
Wireless light delivery systems for subcutaneous phototherapy	✔	✔	Incompatible • *Lack of transparency*	✔ (Fig. 3)
Wireless optogenetic electronics for optogenetics	✔	✔	✔	✔ (Fig. 4a-f)
Delicate bioresorbable optical filters for fluorescence-based neuron imaging	Incompatible • *Lack of bioresorbablity* • *Compression required*	Incompatible • *Compression required*	Incompatible • *Lack of transparency* • *Lack of bioresorbability*	✔ (Fig. 4g-i)
Interconnects/cables	Incompatible • *Compression required* • *Lack of selective adhesion*	Incompatible • *Compression required* • *Lack of encapsulating coating strategy*	Incompatible • *Lack of selective adhesion*	✔ (Fig. 4j-l)
Wireless, miniaturized cardiac pacemakers	Incompatible • *Compression required* • *Inability to bond to device surfaces*	Incompatible • *Compression required* • *Lack of encapsulating coating strategy*	✔	✔ (Fig. 5)
Ultra-thin flexible multielectrode arrays	Incompatible • *Compression required* • *Inability to bond to device surfaces* • *Lack of interface layer strategy*	Incompatible • *Compression required*	✔	✔ (Fig. 6)

3D electronic/photonic systems	Incompatible • *Incompatibility with highly structured and curved surfaces* • *Inability to bond to device surfaces*	Incompatible • *Incompatibility with highly structured and curved surfaces*	Incompatible • *Lack of transparency*	✔ (Extended Data Fig. 1 & Supplementary Fig. 3)

Supplementary Figures

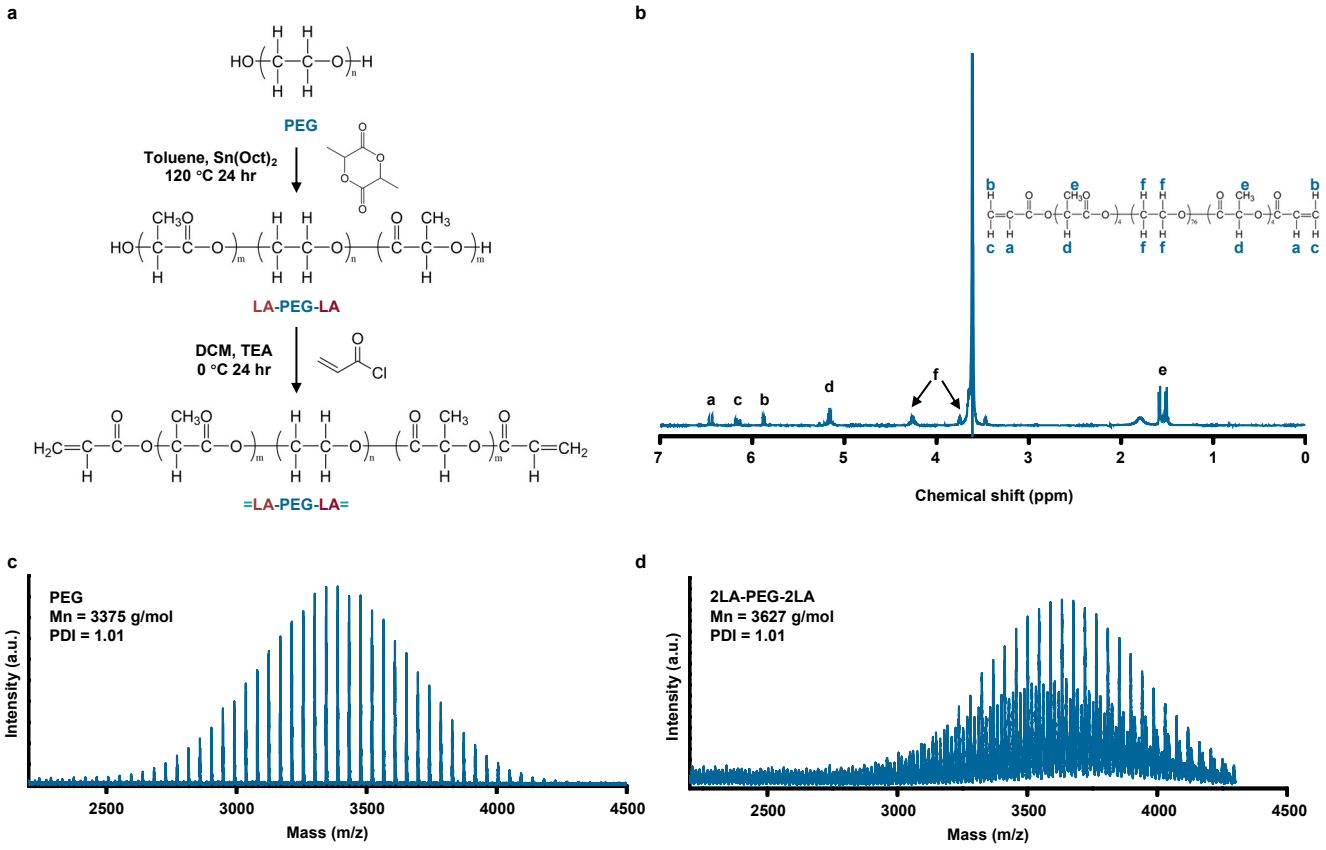

Supplementary Fig. 1 | Synthesis of PEG-LA-DA and chemical characterization. a, The procedures of synthesizing polyethylene glycol-polylactide (PEG-xLA; x = 2, 4, and 10), and further synthesis of PEG-xLA-diacrylate (PEG-xLA-DA, x = 2, 4, and 10). **b,** ^{1}H NMR spectroscopy results for PEG-4LA-DA (MW: ~ 3,350 g/mol). Peak d and e indicate the existence of the lactide acid units, and peak a, b, and c indicate the existence of the acrylate groups in the macromer. **c, d,** Matrix-assisted laser desorption/ionization-time of flight (MALDI-ToF) MS results for (**c**) PEG (nominal MW = 3,350 g/mol) and (**d**) PEG-2LA.

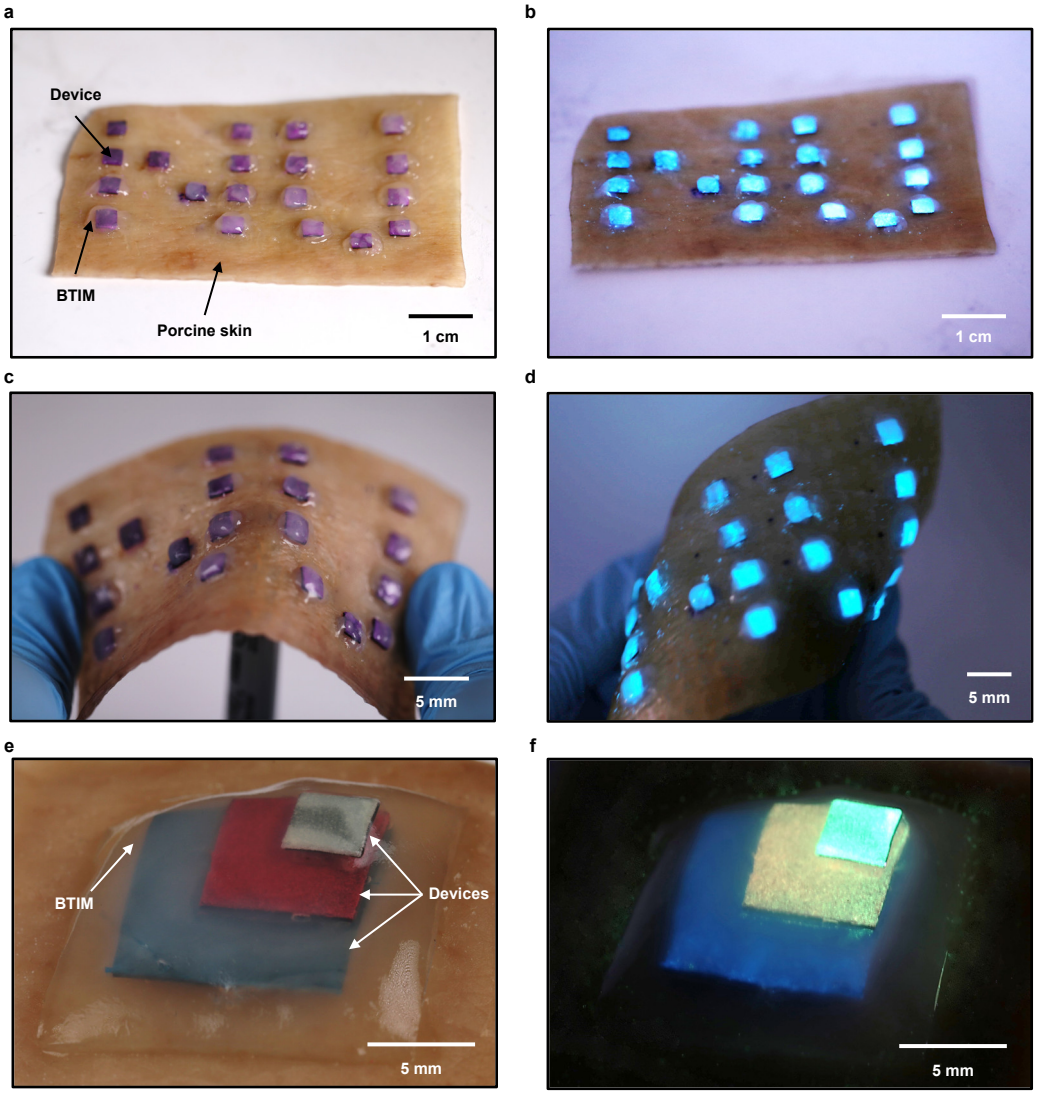

Supplementary Fig. 2 | Integration with device arrays and multilayer configurations. a-d, The BTIM (thickness: 500 μm) anchors multiple components (silicon component coated with a layer of neon fluorescent acrylic paint; size: 4 mm × 4 mm × 500 μm; number: 19) onto a piece of porcine skin using the encapsulation strategy in the shape of 'NU', in a manner that is robust to bending (**c**) and twisting (**d**). **e-f,** Repeating the process with the encapsulation strategy results in a three-layer system.

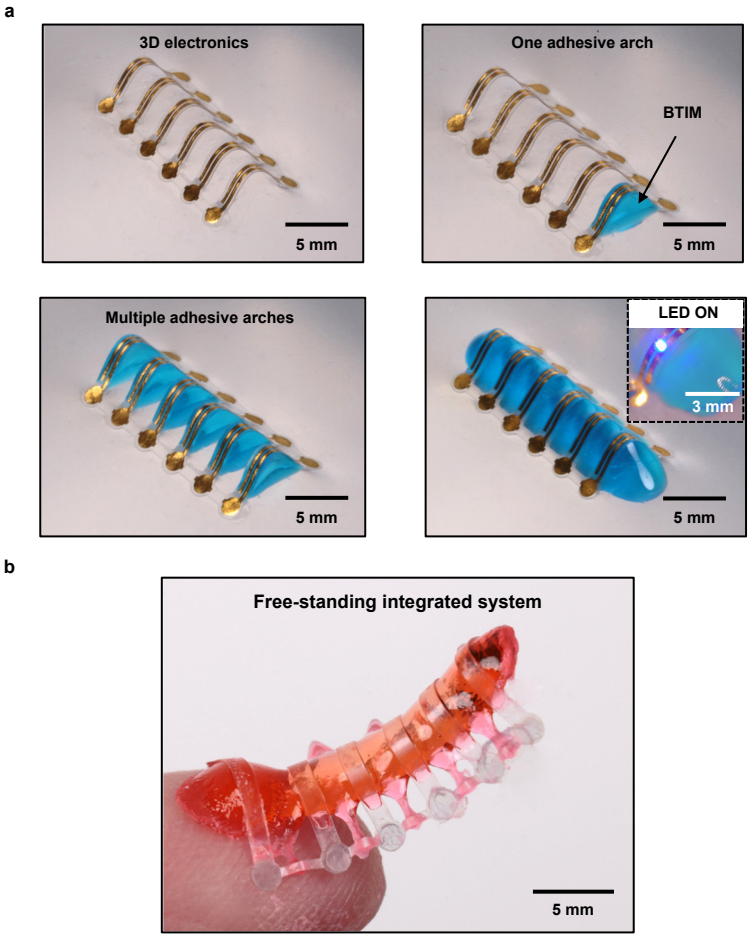

Supplementary Fig.3 | Supporting matrices for electrode-exposed 3D electronic systems. a, Capillary interactions lead to the filling of the BTIM into the interior spaces of the 3D architectures (BTIM dyed in blue). **Inset:** Demonstration of such a device with an operating μ-ILED. **b,** Free-standing electrode-exposed electronic system (BTIM dyed in red).

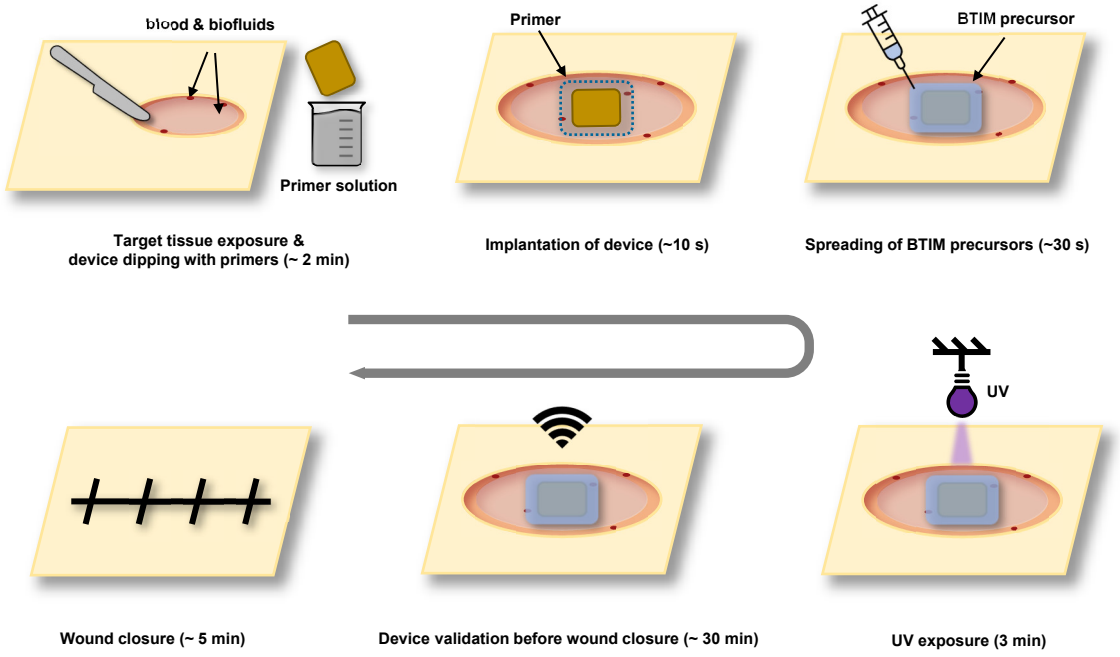

Supplementary Fig. 4 | Procedures for implanting BTIM-integrated devices *in vivo*. BTIM precursors are designed to spread onto devices/tissues within 30 min after applying primers onto the surfaces of the devices, to minimize the extent of hydrolysis of the coupling reagents (EDC and Sulfo-NHS) in the primer solutions and consequent reductions in interfacial bonding strength. The BTIM can be used as either encapsulating coatings, interfacial layers, or supporting matrices. For the encapsulating coating and supporting matrix strategies, the UV exposure process is not affected by the opacity of the devices since the precursors occupy mainly a space on top of the devices. For the interfacial layer strategy, to avoid the effects of device shadowing, a substantial area of the device should be fully or partially transparent to UV light. Application of primers onto the electronics surfaces before implantation represents a key part of the process flow for fabricating the devices. Soaking the devices in the primer solutions before implantation yields a uniform liquid-type primer layer.

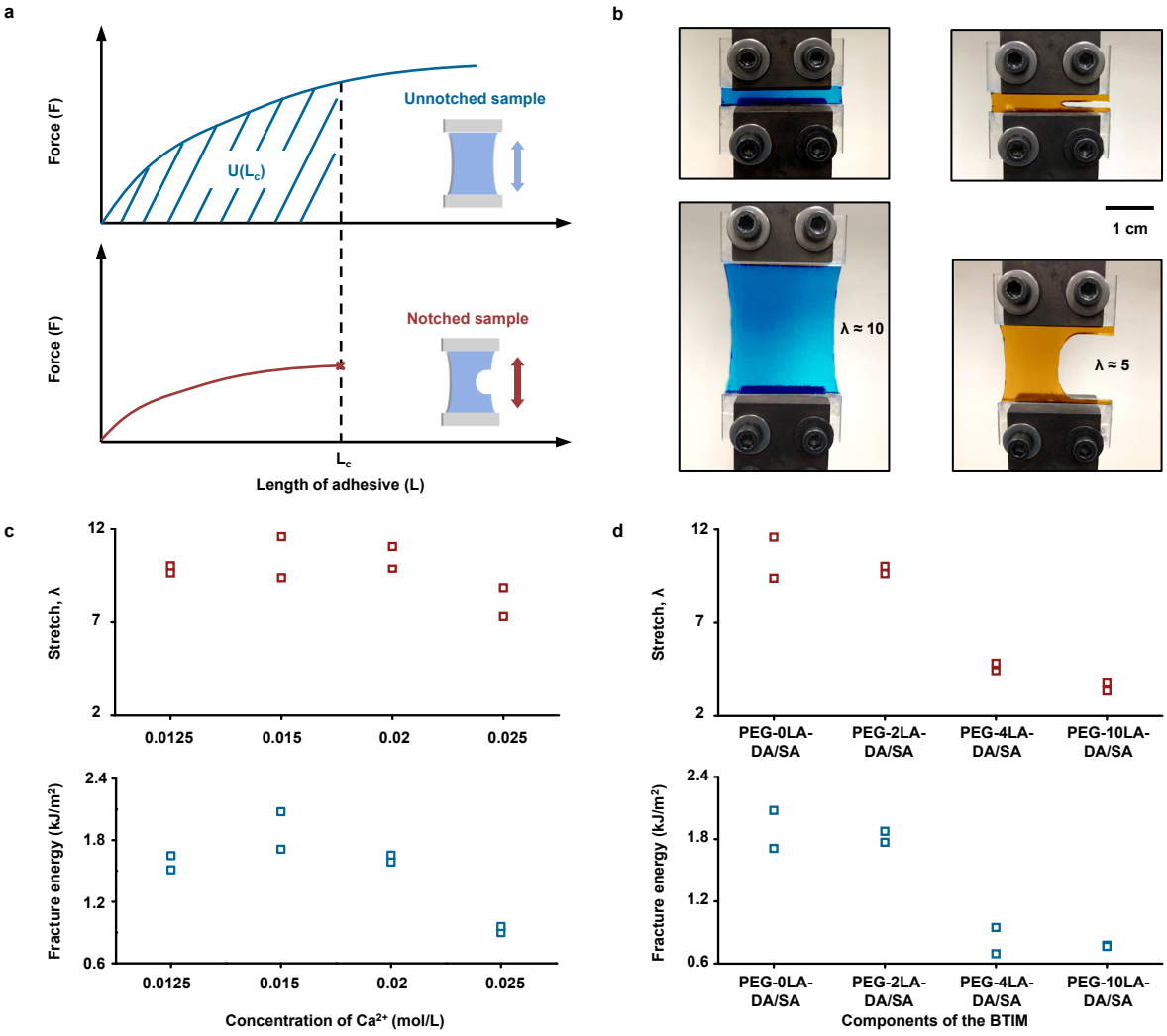

Supplementary Fig. 5 | Fracture energy and elongation of the BTIM. a, Strategy to measure fracture energy of BTIM samples. The area under the stress/strain curve for unnotched specimens up to the strain at initial crack propagation defines the fracture energy. **b,** The unnotched (first panel; colored in blue; 50 mm × 5 mm × 2 mm) and notched specimens (second panel; colored in orange; 50 mm × 5 mm × 2 mm ; notch length: 25 mm) can be stretched up to 8 and 5 times, respectively. **c,** Maximum elongation (first row) and fracture energy (second row) for different concentrations of Ca^{2+} as the ionic crosslinker for the alginate network (Ca^{2+} concentration: 1.25, 1.5, 2.0, 2.5 %). **d,** Maximum elongation (first row) and fracture energy (second row) for different lactide repeat units on each end of the PEG (PEG-xLA-DA, x is 0, 2, 4, and 10).

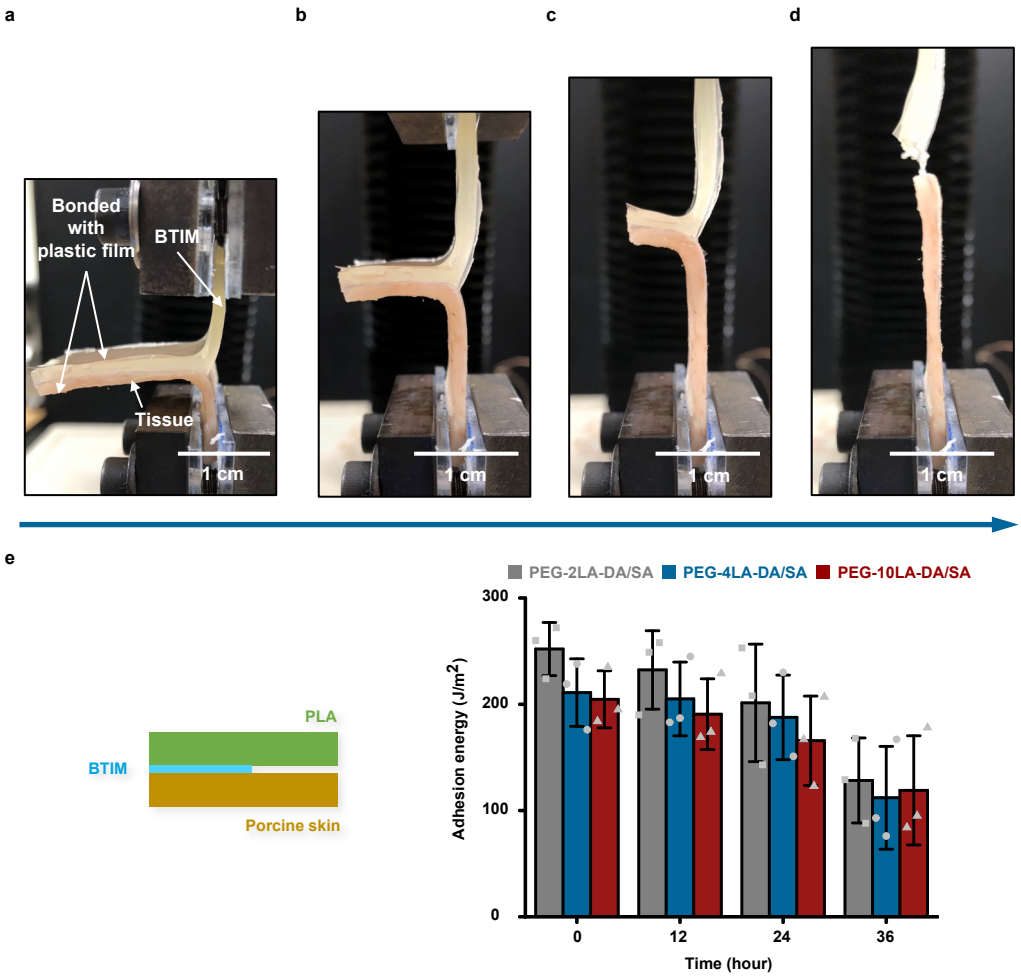

Supplementary Fig. 6 | Adhesion measurements and *in vitro* evaluations. a, Setup for peel tests. Bonding both the BTIM and the porcine skin to sheets of PLA (thickness: 50 μm) eliminates any significant energy dissipation from elastic deformations of the BTIM and the porcine skin. **b-d,** Representative images during the peeling process at displacements of 5.4, 11.1, and 18.4 mm, respectively. **e,** Soaking a tri-layer structure (PLA/BTIM/porcine skin; thickness: 50/100/1500 μm) in phosphate-buffered saline (PBS; pH 7.4) at 37 °C indicates stable adhesion strength within experimental uncertainties for 24 h. The BTIMs with 2, 4, and 10 lactide acid units, respectively, present similar behaviours over 36 hours. $n = 3$ independent samples in **e**. Values in **e** represent the mean ± standard deviation.

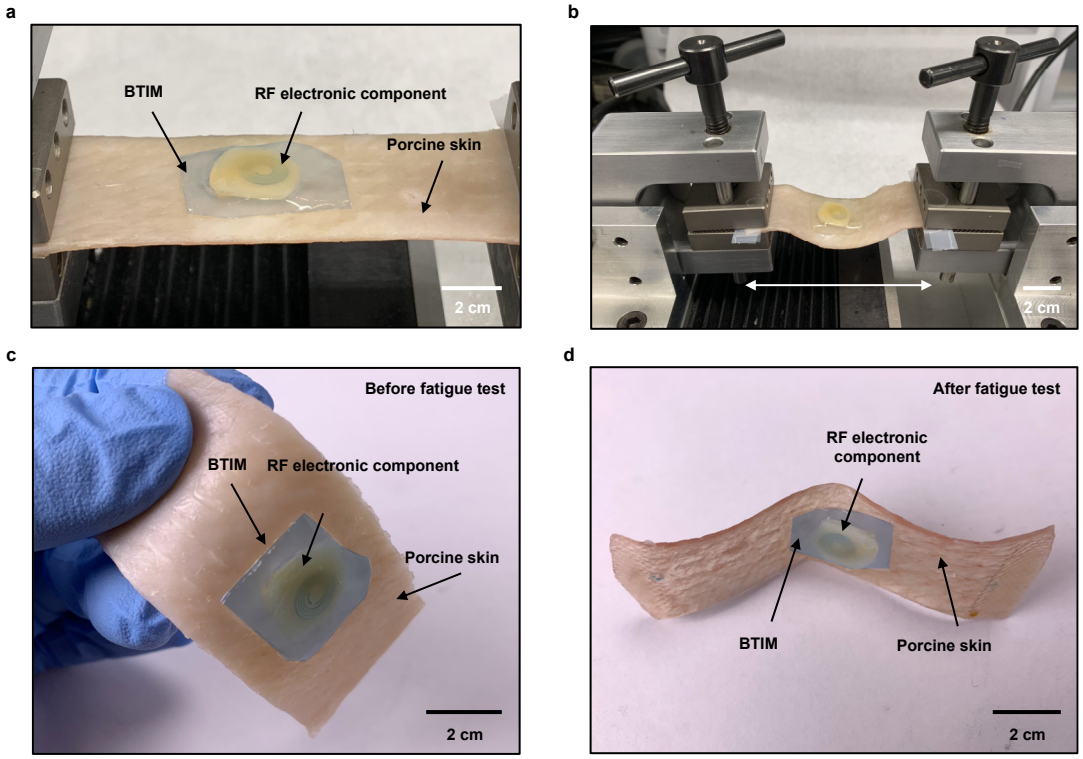

Supplementary Fig. 7 | Stretching fatigue tests of a radio frequency (RF) electronic device. a, Anchoring the device (Candelilla wax/Mo/Candelilla wax; thickness: 300/50/300 μm; resonance frequency: ~ 300 MHz) onto a piece of porcine skin by the BTIM (thickness: ~ 1 mm) using the encapsulation strategy. **b,** Images of the fatigue setup. The ends of the porcine are fixed with clamps, and the fatigue tests involve 4 × 10^4 cycles with a maximum strain of 10 %. The overall setup is maintained under a moist environment. **c, d,** Photographs of the entire system before (**c**) and after (**d**) fatigue tests. Even if the porcine skin dries after the fatigue test, the bonding persists without significant delamination. The BTIM is colored in blue for better visualization.

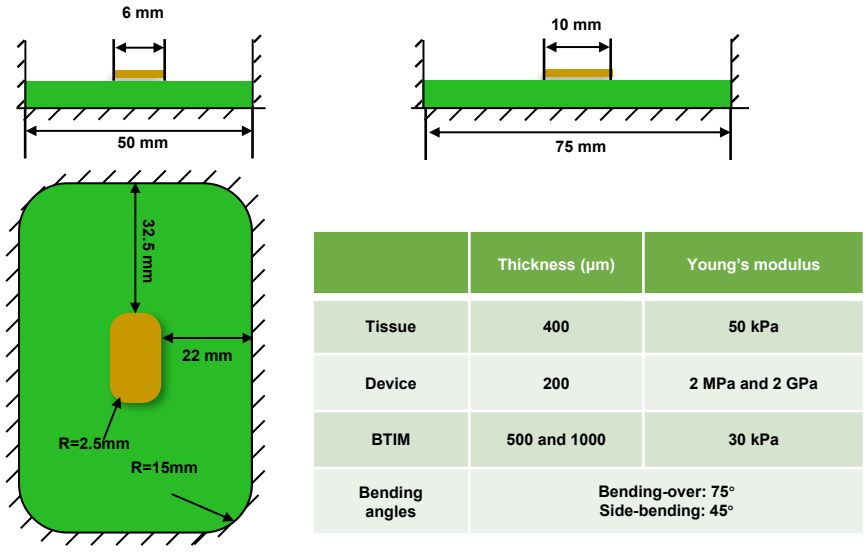

	Thickness (μm)	Young's modulus
Tissue	400	50 kPa
Device	200	2 MPa and 2 GPa
BTIM	500 and 1000	30 kPa
Bending angles	Bending-over: 75° Side-bending: 45°	

Supplementary Fig. 8 | Parameters for finite element analysis. Drawings of the working conditions and related parameters. Inset table: thickness and Young's modulus of each material.

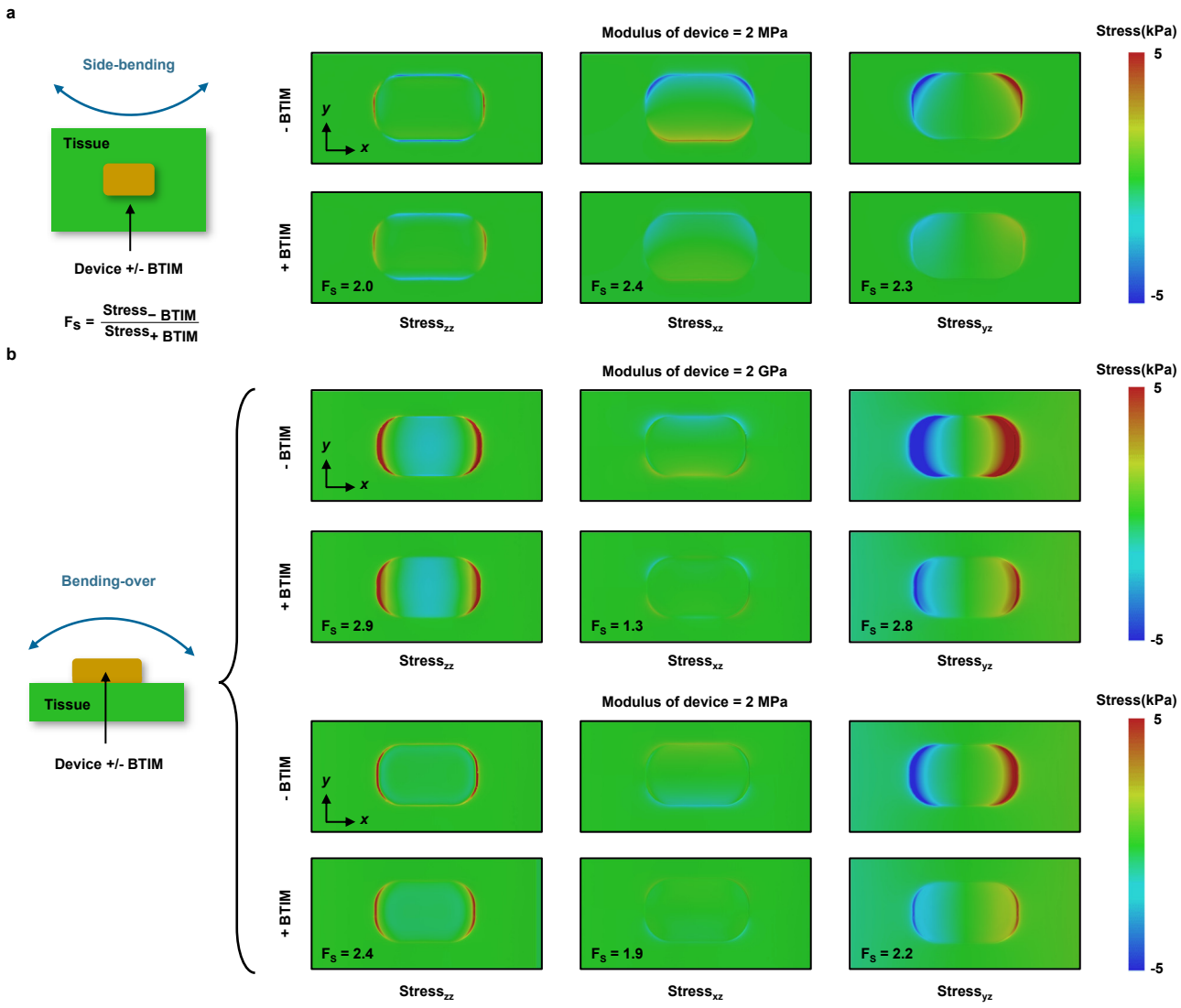

Supplementary Fig. 9 | Effects of modulus on distribution of normal and shear stresses. a, Distribution of normal and shear stresses at the interfaces of tissue and devices with different modulus associated with natural motions under side-bending deformation (angle: 45°). **b,** Distribution of normal and shear stresses at the interfaces of tissue and devices with different modulus associated with natural motions under bending-over deformation (angle: 75°).

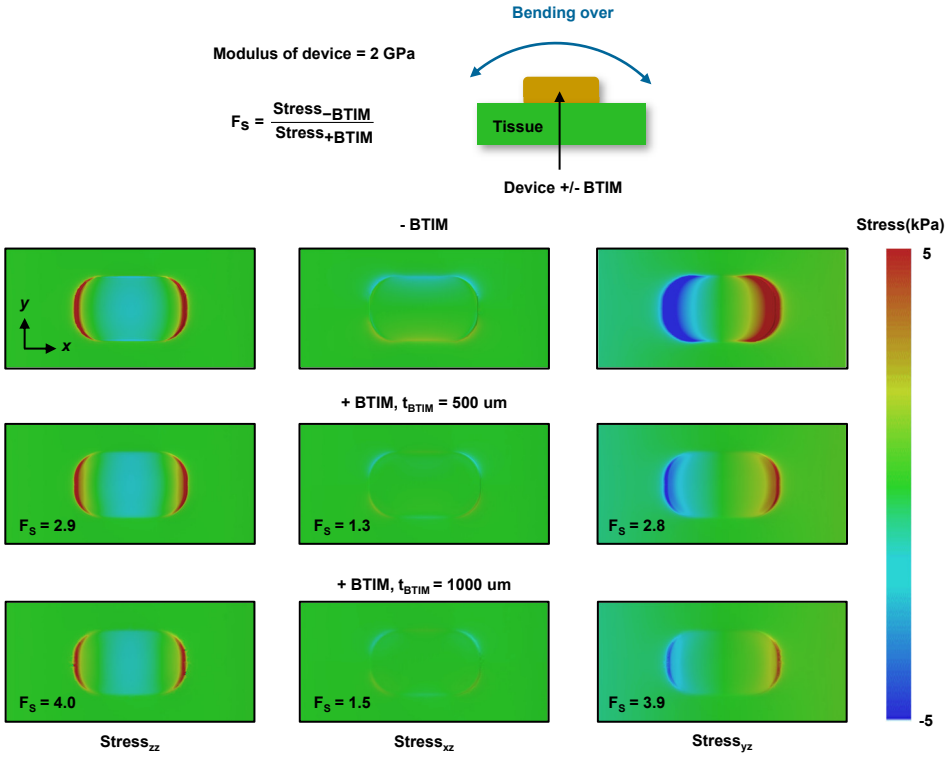

Supplementary Fig. 10 | Effects of thickness on distribution of normal and shear stresses. The thicknesses of the BTIM are 500 μm and 1000 μm for the second and third rows, respectively (bending-over motion, angle: 75°; E_{device} = 2 GPa).

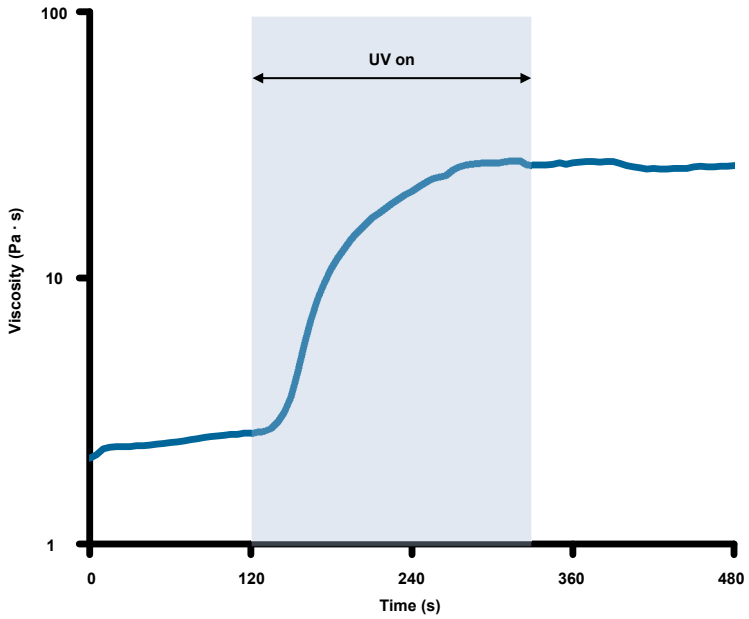

Supplementary Fig. 11 | Viscosity of the BTIM during the photoinitiated transformation. The initial viscosity of the BTIM precursors is ~ 2 – 3 Pa•s. UV exposure occurred from 120 s to 300 s to complete the transformation. The viscosity and modulus increase by another factor of ten or more during this period, to stabilize the material as a soft solid.

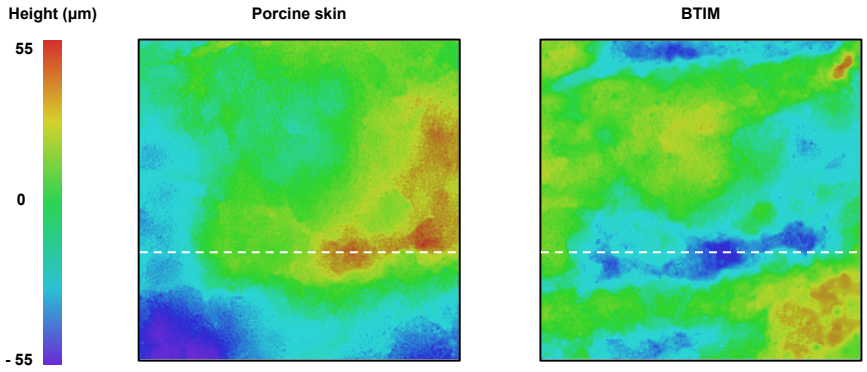

Supplementary Fig. 12 | Surface morphology of skin and BTIM. The surface profile includes a piece of porcine skin and a piece of the BTIM cast and subsequently removed on this skin.

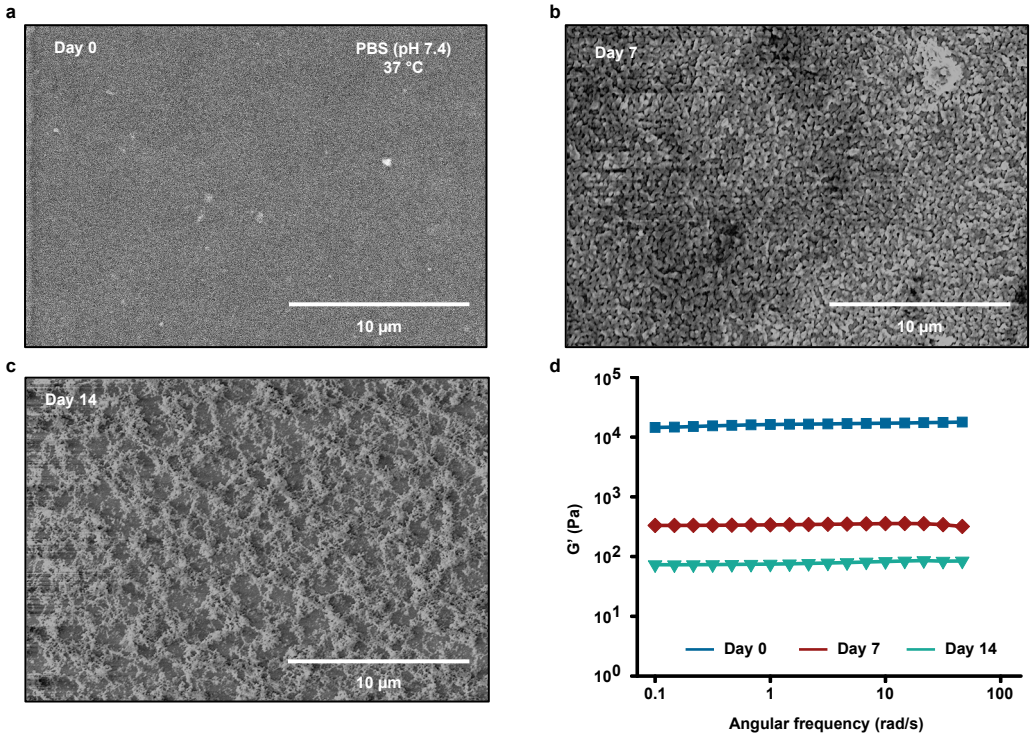

Supplementary Fig. 13 | Degradation behaviors of the BTIM. a-c, Microstructures of the BTIM based on PEG-2LA-DA on day 0, 7, and 14 after immersion in PBS (pH 7.4) at 37 °C. The BTIM becomes porous and rough during degradation. **d,** The storage modulus (*G'*) as a function of immersion time.

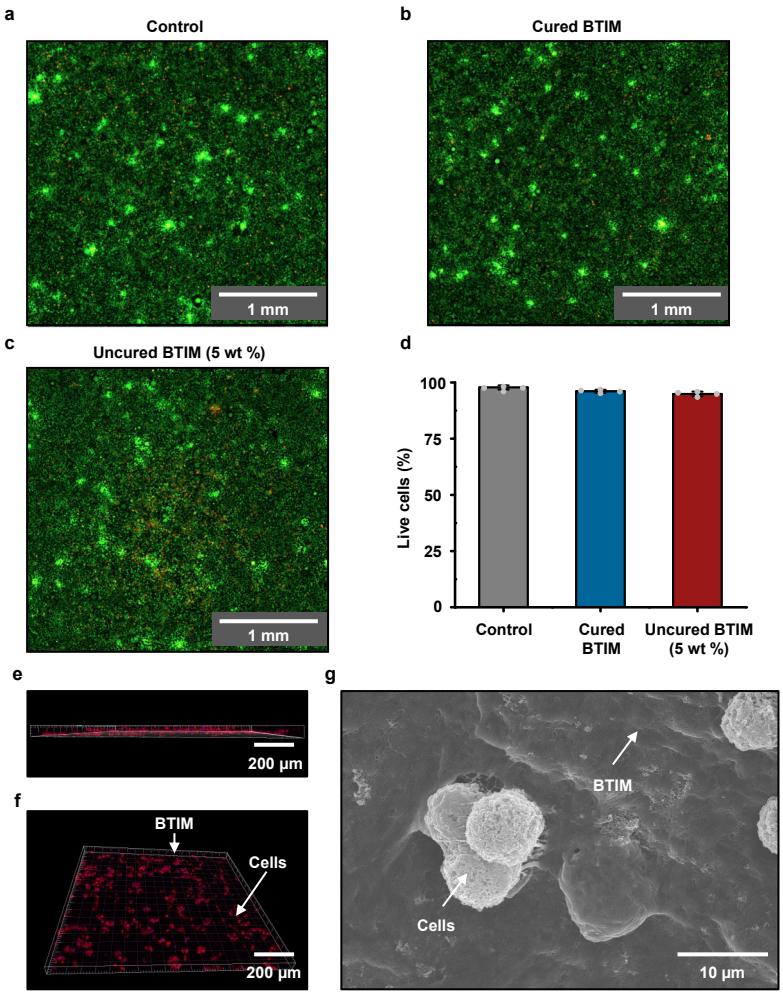

Supplementary Fig. 14 | Tests of cytotoxicity. a-c, Images of L929 live/dead cells for the control group (**a**), cured BTIM (5-mm-diameter; thickness: ~ 0.5 mm, **b**), and BTIM precursors (5 wt % in cell culture media, **c**). **d,** Statistic analyses of cell viability by the percentages of live cells L929 for the control group, cured BTIM (5-mm-diameter; thickness: ~ 0.5 mm), and BTIM precursors (5 wt % in cell culture media). **e, f,** Confocal images of cells (red) migrating in a piece of the BTIM. **g,** SEM image of cells migrating into a piece of the BTIM. $n = 4$ independent measurements in **a-d** and $n = 3$ independent measurements in **e-g**. Values in **d** represent the mean ± standard deviation.

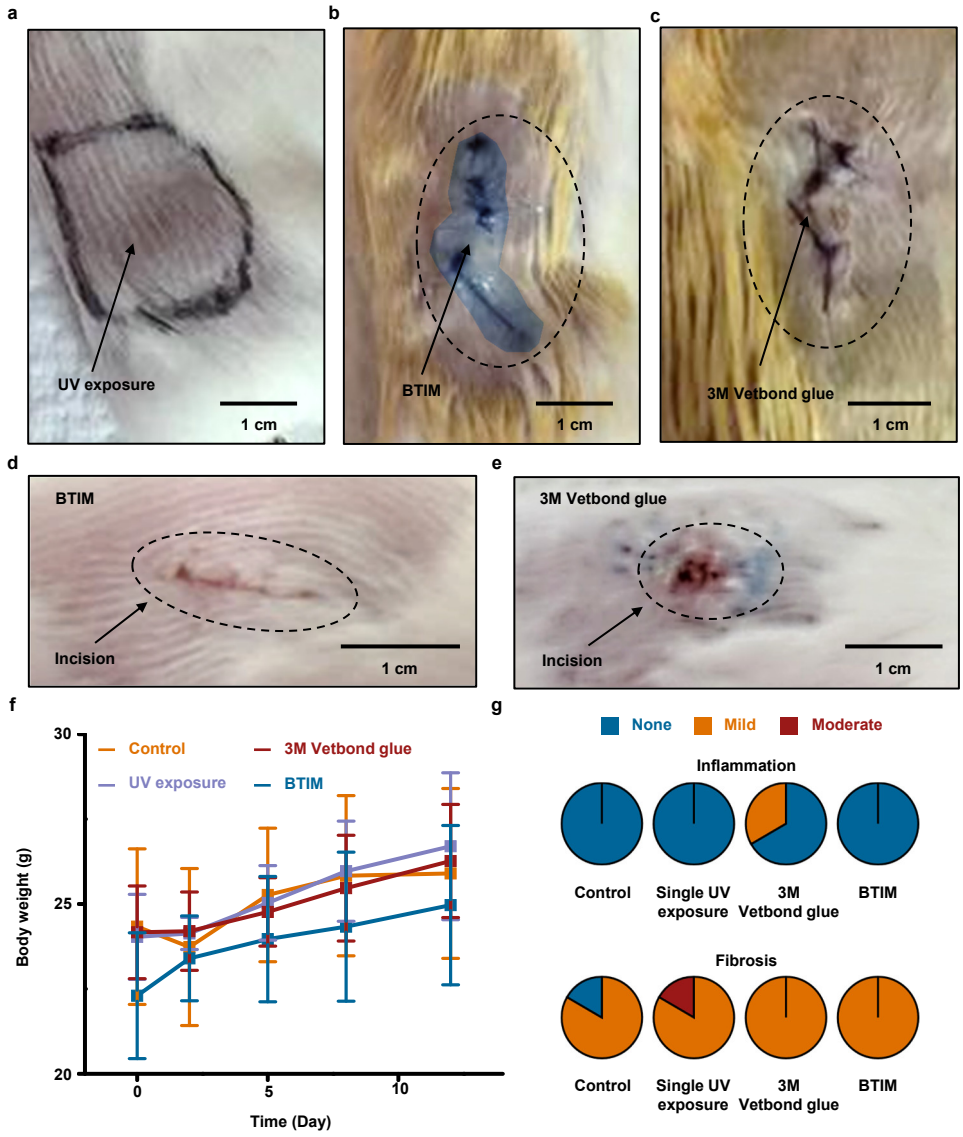

Supplementary Fig. 15 | *In vivo* biocompatibility of the BTIM. a, Skin with UV exposure. **b,** Skin with a surgical site incision closed by a layer of the BTIM (colored in blue). **c,** Skin with a surgical site incision closed by Vetbond tissue glue (3M, USA). The length of the surgical site incision is ~ 15 mm. **d, e,** Wound-healing behaviors with the BTIM (**d**) and Vetbond glue (**e**) on day 5 post-surgery. **f,** Body weights of animal subjects within 2 weeks. **g,** Histological evaluations of samples of skin tissue by a double-blinded clinical-scoring system on a scale of 0 to 5 to determine the level of inflammation (first row) and fibrosis (second row) in each group after 2 weeks post-surgery. $n = 3$ biologically independent animals. Values in **f** represent the mean ± standard deviation.

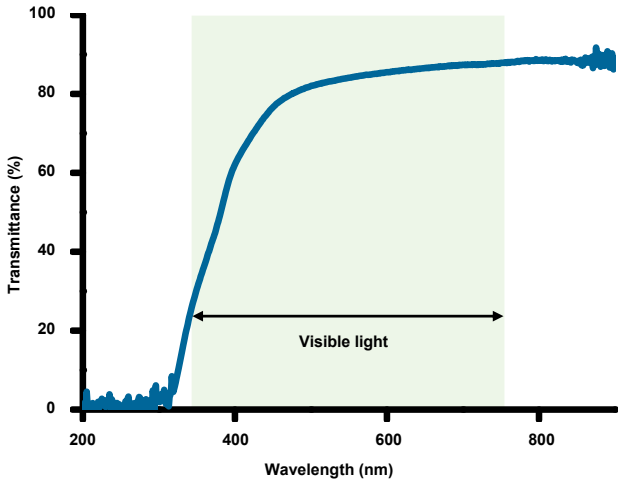

Supplementary Fig. 16 | Transmittance of the BTIM. The transmittance is between 60 – 80 % in the range of 395 to 475 nm, and remains higher than 80 % between 475 – 900 nm. The thickness of the samples is 1 mm.

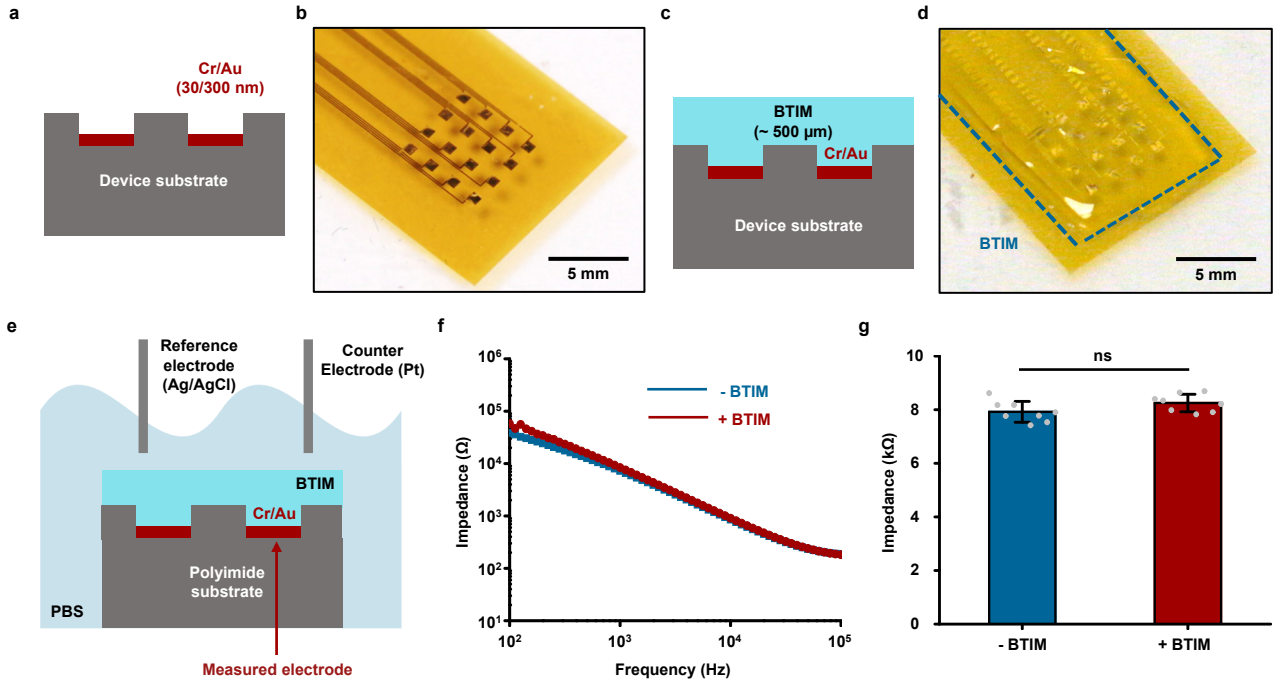

Supplementary Fig. 17 | Effects of electrical conduction on device performance. a, b, Schematic illustration (**a**) and photograph (**b**) of the MEA device (polyimide/Cr/Au/parylene: 4 µm/30 nm/300 nm/4 µm) under test. **c, d,** Schematic illustration (**c**) and photograph (**d**) of the BTIM-encapsulated MEA device (BTIM thickness: ~ 500 µm). **e,** Schematic illustration of the setup to measure the impedance of the MEA electrodes. **f,** Representative impedance spectra of an MEA electrode before (blue) and after (red) BTIM application in 0.1 M PBS at room temperature. **g,** Statistical results for impedance values before and after BTIM application at 1 kHz in 0.1 M PBS at room temperature ($P = 0.0884$). $n = 8$ independent samples in **g**. Values in **g** represent the mean ± standard deviation. Statistical significance and P values are determined by two-sided Student's t-test at a significance level of 0.05. ns indicates no statistically significant differences.

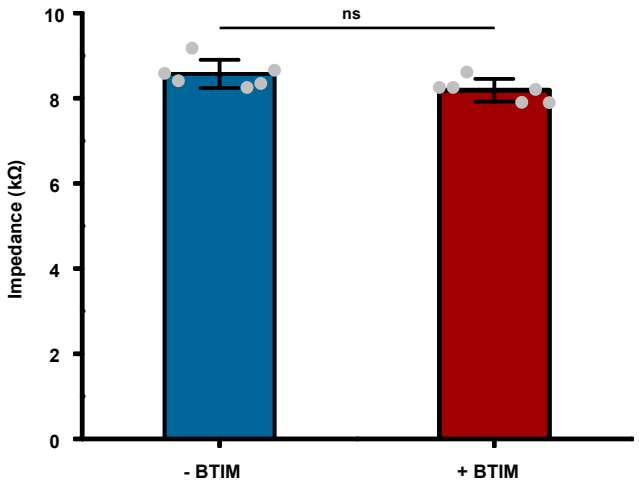

Supplementary Fig. 18 | Statistical results before and after BTIM application. The statistical results are from the impedance spectra between two adjacent MEA electrodes before (blue) and after (red) BTIM application at 1 kHz in 0.1 M PBS at room temperature (P = 0.0523). $n = 6$ independent samples. Values represent the mean ± standard deviation. Statistical significance and P values are determined by two-sided Student's t-test at a significance level of 0.05. ns indicates no statistically significant differences.

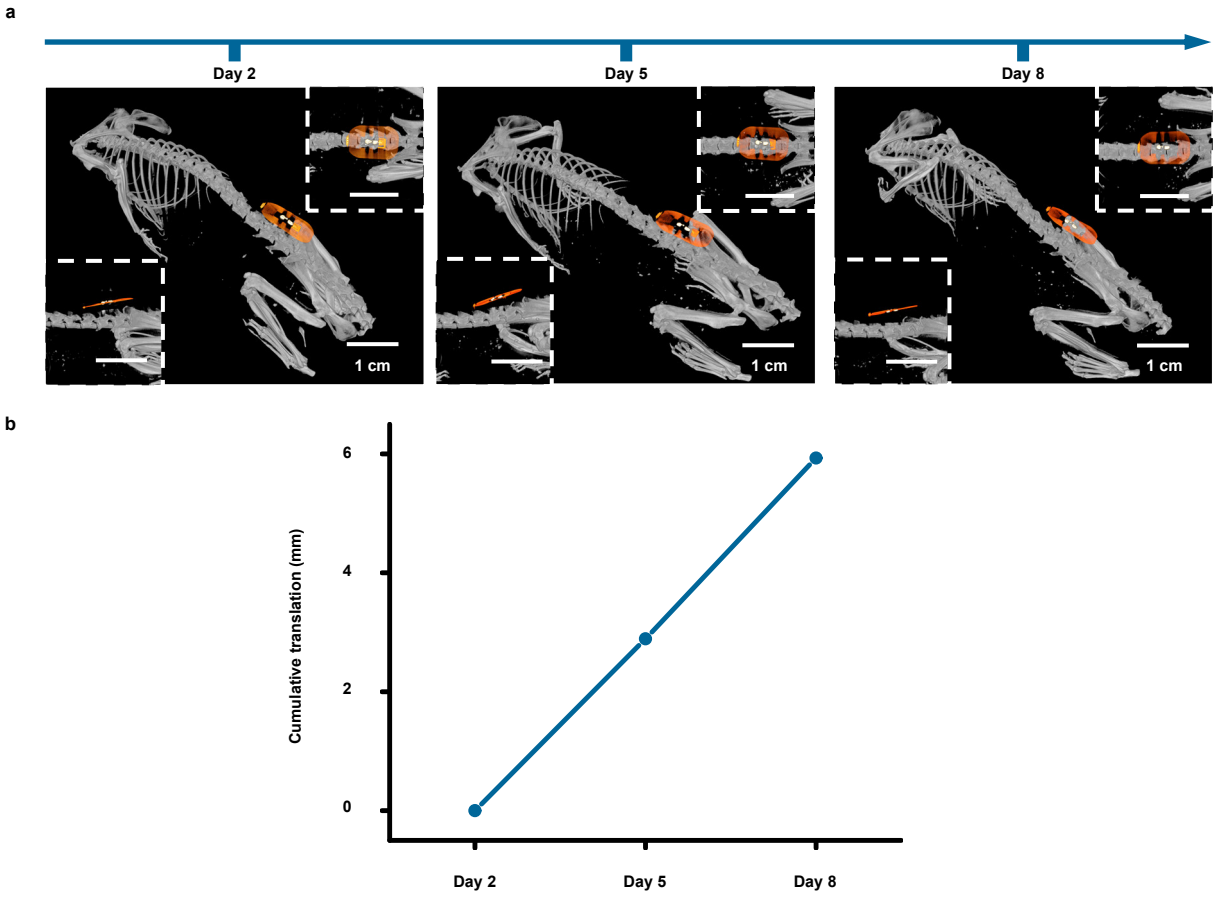

Supplementary Fig. 19 | Measurements of translation of a device implanted using the BTIM with the interface strategy. a, Positions of devices integrated with an interface layer of the BTIM (12 mm × 8 mm × 500 μm) in diagonal (main), sagittal (first inset), and coronal (second inset) directions across day 2, 5 and 8 post-surgery determined by micro-computed tomography (MicroCT). **b,** Line chart of the cumulative translations of devices integrated with an interface layer of the BTIM, as a function of time.

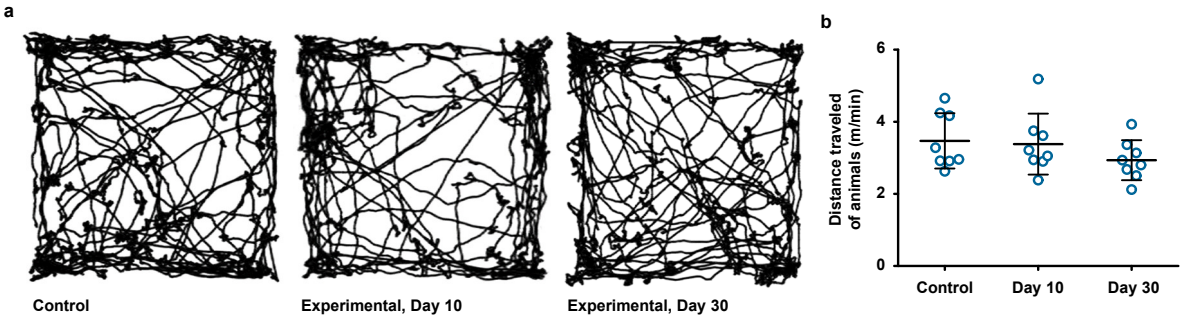

Supplementary Fig. 20 | Motion tracking in mice on day 10 and day 30 post-surgery. a, Results of control and experimental groups on day 10 and day 30 post-surgery (5 min recording in a rectangular arena). **b,** Results on these two groups are the same within experimental uncertainties. $n = 8$ independent animals. Values in **b** represent the mean ± standard deviation.

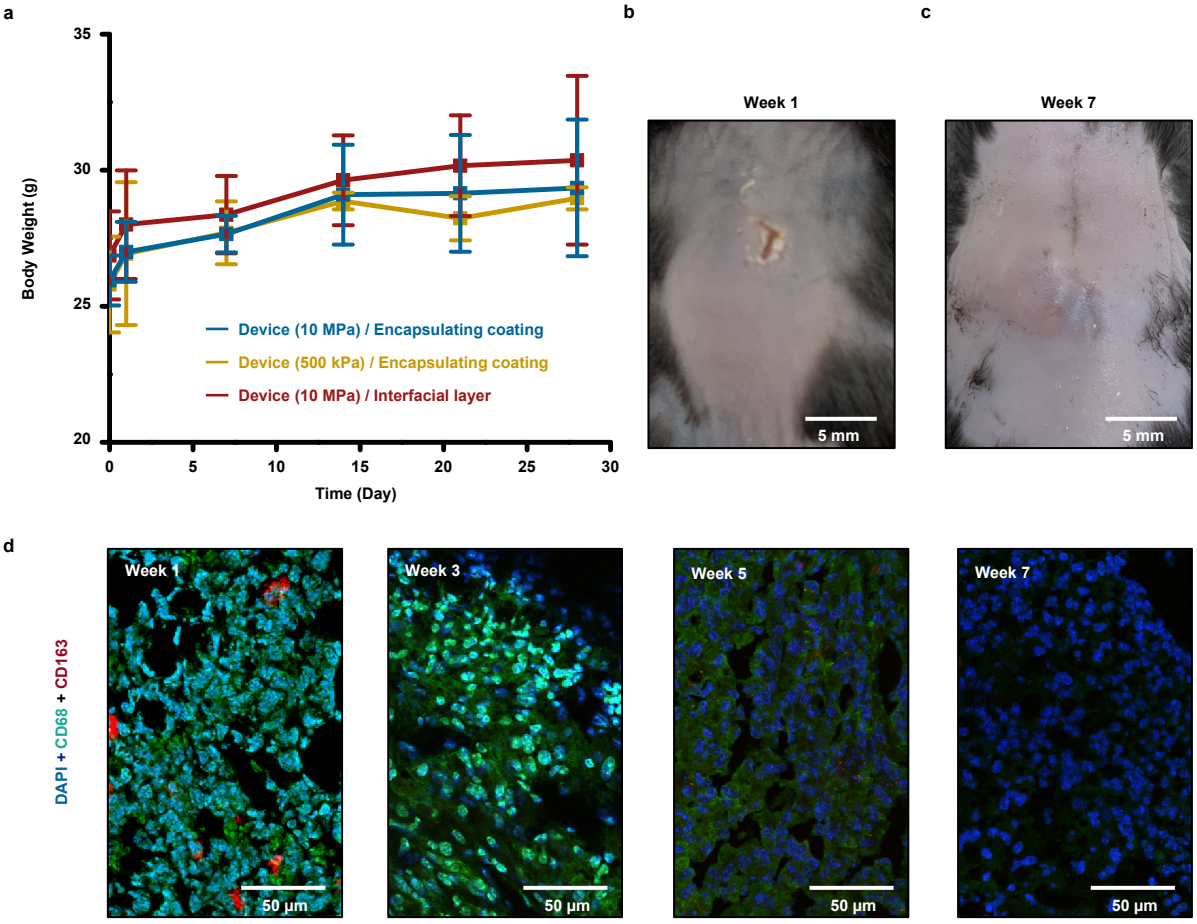

Supplementary Fig. 21 | Wound-healing behaviors after back subcutaneous implantation. a, Body weights of experimental mice implanted with different devices (500 kPa and 10 MPa) using different BTIM strategies (encapsulating coating and interface layer) for 1 month post-surgery. **b, c,** Photographs of the surgical site wound at week 1 (**b**) and 7 (**c**) post-surgery for an animal implanted with an encapsulated soft device in the subcutaneous area (modulus: 10 MPa). The wound mostly heals 1 week post-surgery, leaving only a sanguineous crust. On week 7, the wound completely heals. **d,** Immunohistochemical staining of subdermal tissues collected at 1, 3, 5, and 7 weeks post-surgery reveals comparable monocyte (CD68+, green) and leukocyte (CD163+, red) inflammatory cell infiltration at the adhesive-tissue interface. The nucleus is labelled in blue using 4',6-diamidino-2-phenylindole (DAPI). $n = 3$ biological independent animals in **a-c** and $n = 4$ biological independent animals in **d**. Values in **a** represent the mean ± standard deviation.

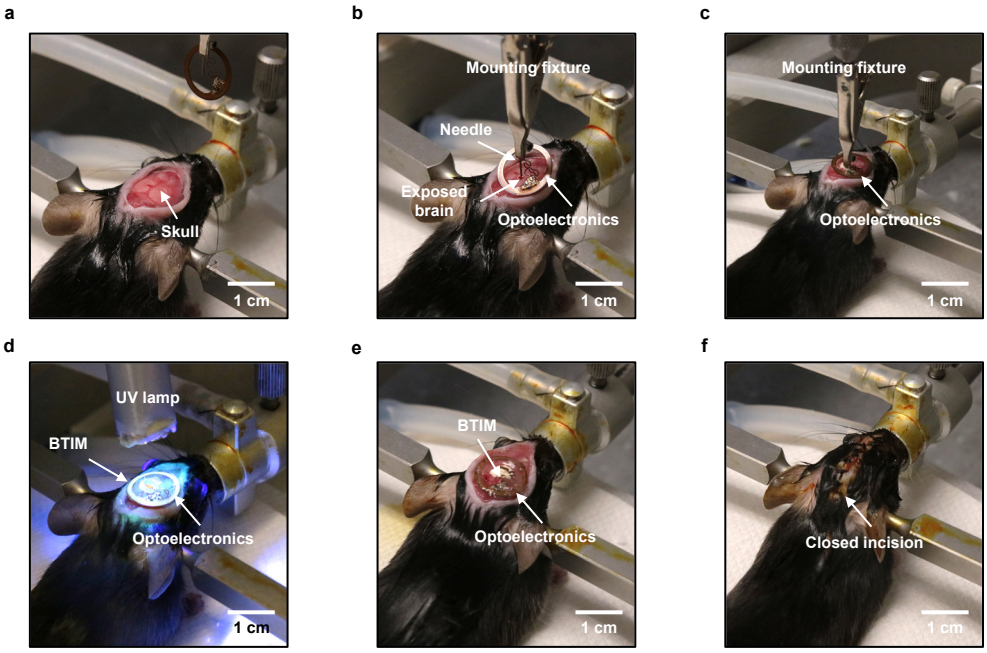

Supplementary Fig. 22 | Surgical procedures for implanting wireless optogenetic devices. a, Exposing the skull with a 5-mm-long incision made on the scalp. **b,** Drilling a hole on the skull to expose the brain for inserting the probe into the targeted brain regions. **c,** Placing the receiver coil and interconnects on the skull. **d,** Applying primers and precursors, followed by UV exposure. **e,** Curing the BTIM and anchoring the receiver coil and interconnects on the skull. **f,** Closing the wound on the skin.

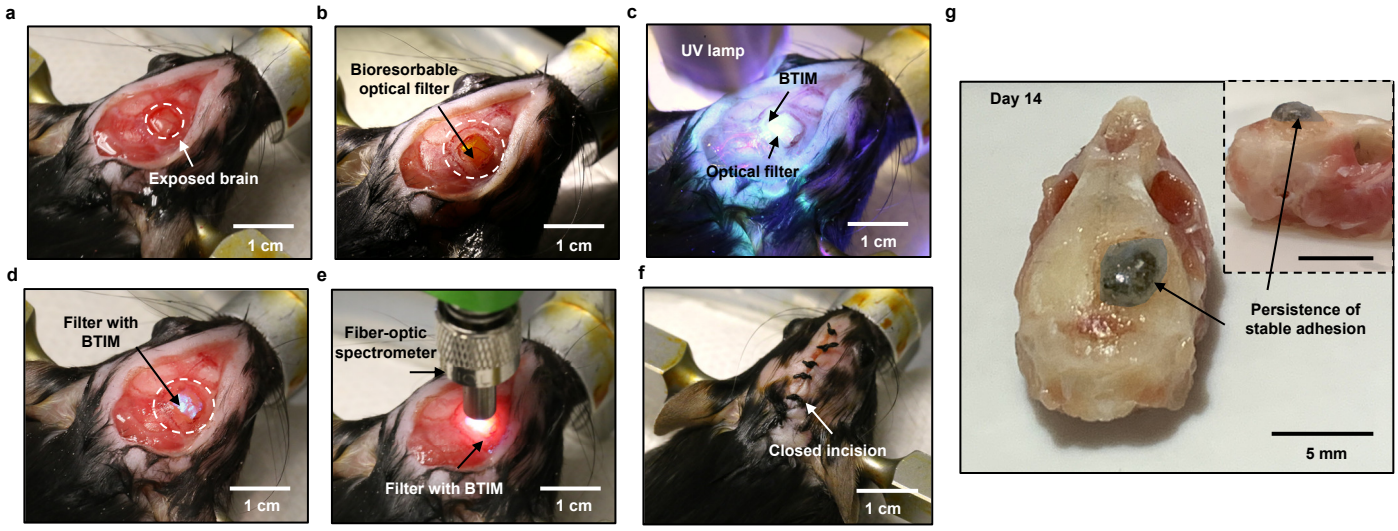

Supplementary Fig. 23 | Surgical procedures for bioresorbable optical filters. a, Exposing the skull with a 5-mm-long incision made on the scalp to drill a hole (diameter: ~ 2 mm) on the skull to expose the brain. **b,** Applying such an optical filter above the exposed brain. **c,** Applying primers and precursors, followed by UV exposure. **d,** Curing the adhesive. **e,** Obtaining transmission spectra after applying the BTIM. **f,** Closing the skin wound. **g,** Stable adhesion persists even after two weeks post-surgery (BTIM colored in blue).

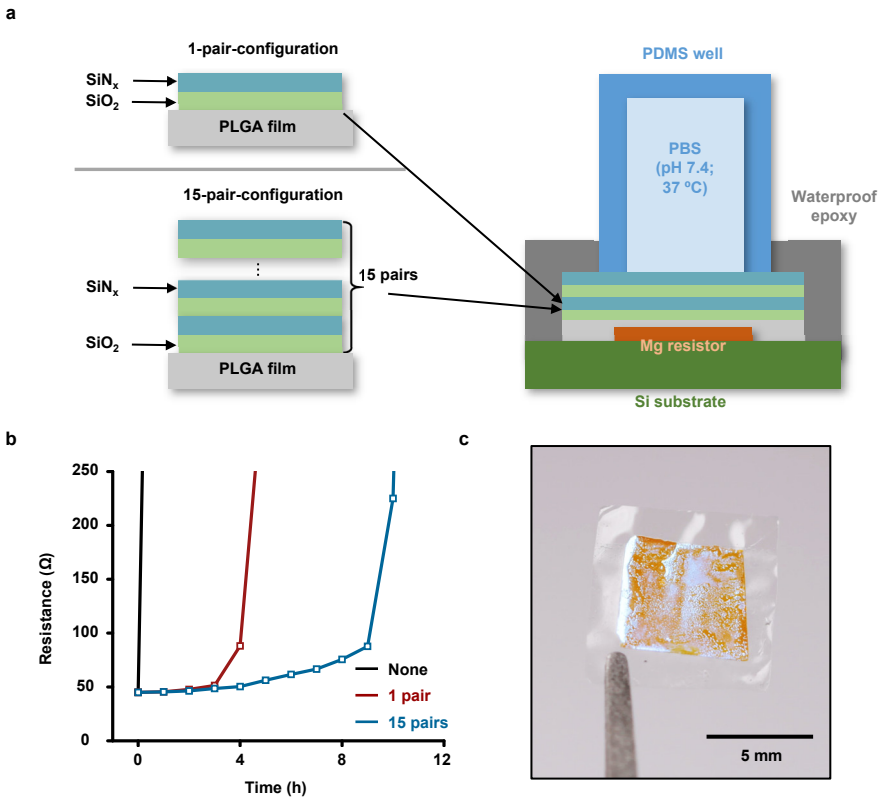

Supplementary Fig. 24 | Performance of multi-pairs of SiO_x and SiN_x layers. a, Experimental set-up designed to test the encapsulation performance of the bi-/multi-layer structure upon immersion in PBS (pH 7.4) at 37 ºC. A patterned thin film trace of Mg (thickness: 300 nm; serpentine length: 1.45 mm; width: 150 μm; turns: 4) formed on a silicon wafer acts as an indicator for water penetration. The bi-/multi-layer structures cover the Mg traces, with the edges sealed by waterproof epoxy. **b,** Representative curves showing changes in resistance as a function of soaking time for non-encapsulated Mg traces and the traces covered with bi-/multi-layer structures. **c,** 15-pair structure, wrapped onto the edge of a glass slide, as an illustration of the mechanical flexibility of the film. The thickness of SiO_x and SiN_x layers are 54 and 85 nm, respectively.

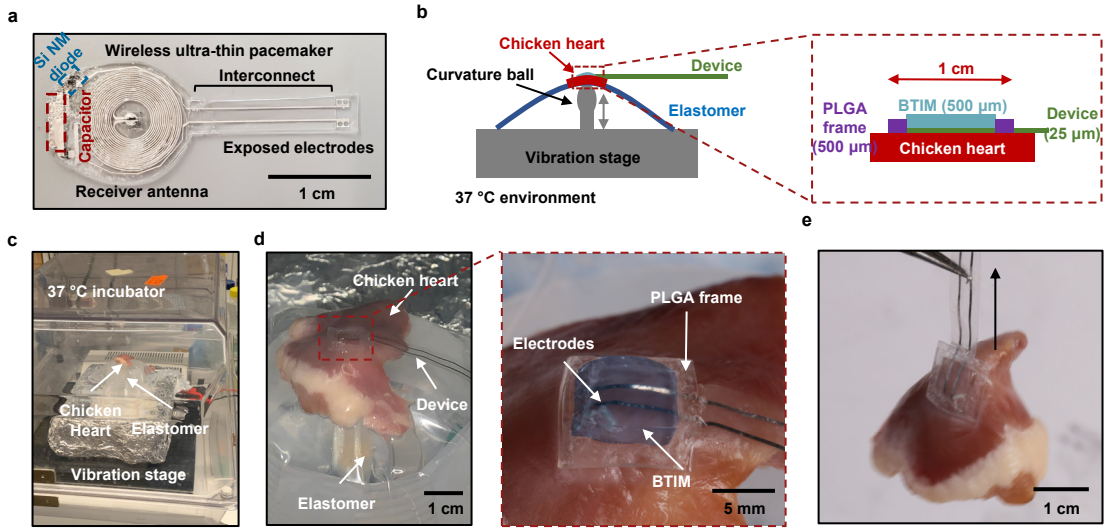

Supplementary Fig. 25 | *Ex vivo* characterization of devices for the epicardium. a, Miniaturized, battery-free, leadless pacemaker for cardiac pacing. The pacemaker consists of three main components – a power receiver antenna for energy harvesting, a pair of electrodes that interface to the myocardium, and an interconnect structure that connects the two. Such a pacemaker only provides electrical stimulation and does not support any sensing capabilities. **b,** Schematic illustration of the *ex vivo* setup. A chicken heart is placed on the vibration stage operating at 20 Hz in the 37 °C incubator. Arching the cardiac tissue provides a curvature similar to that of a rat heart. **c,** Image of the setup. **d,** Image of electrodes encapsulated with the BTIM on the curved heart. Red insert: Anchoring the electrodes with a PLGA frame (8 mm × 8 mm × 500 μm) on the heart using the BTIM (colored in blue). **e,** Hanging and shaking the device loaded by the chicken heart without significant delamination.

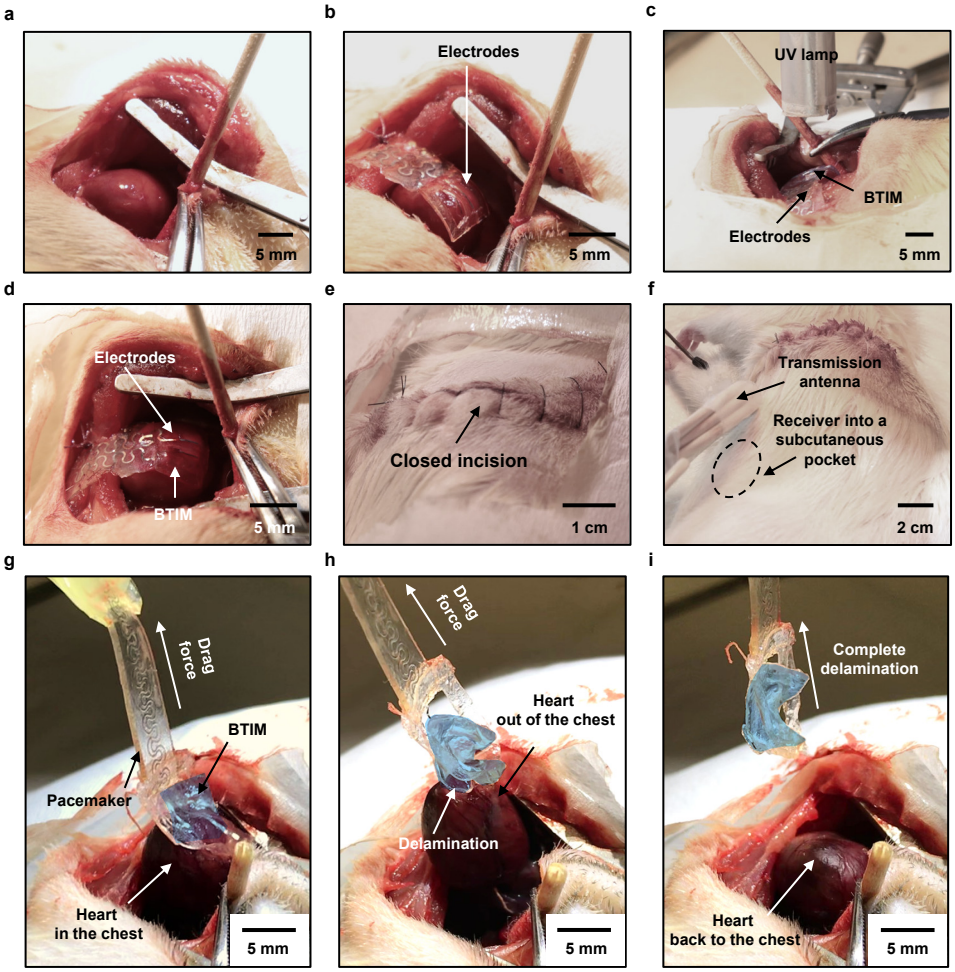

Supplementary Fig. 26 | *In vivo* characterization of adhesion between electrodes and the epicardium. a-f, Surgical procedures for wireless systems designed for cardiac pacing. **a,** Exposing the rat heart via left thoracotomy. **b,** Placing the receiver coil in a subcutaneous pocket on the ventral aspect of the rat and the electrodes with the PLGA/PU frame onto the anterior epicardial surface. **c,** Applying primers and precursors in the area defined by the PLGA/PU frame, followed by UV exposure. **d,** Curing the adhesive to anchor the electrodes to the epicardium. **e,** Closing the incision. **f,** Powering the wireless pacemaker by inductive power transfer using a transmission coil. **g-i,** Images of robust adhesion between electrodes and the heart as provided by the BTIM (colored in blue for better visualization).

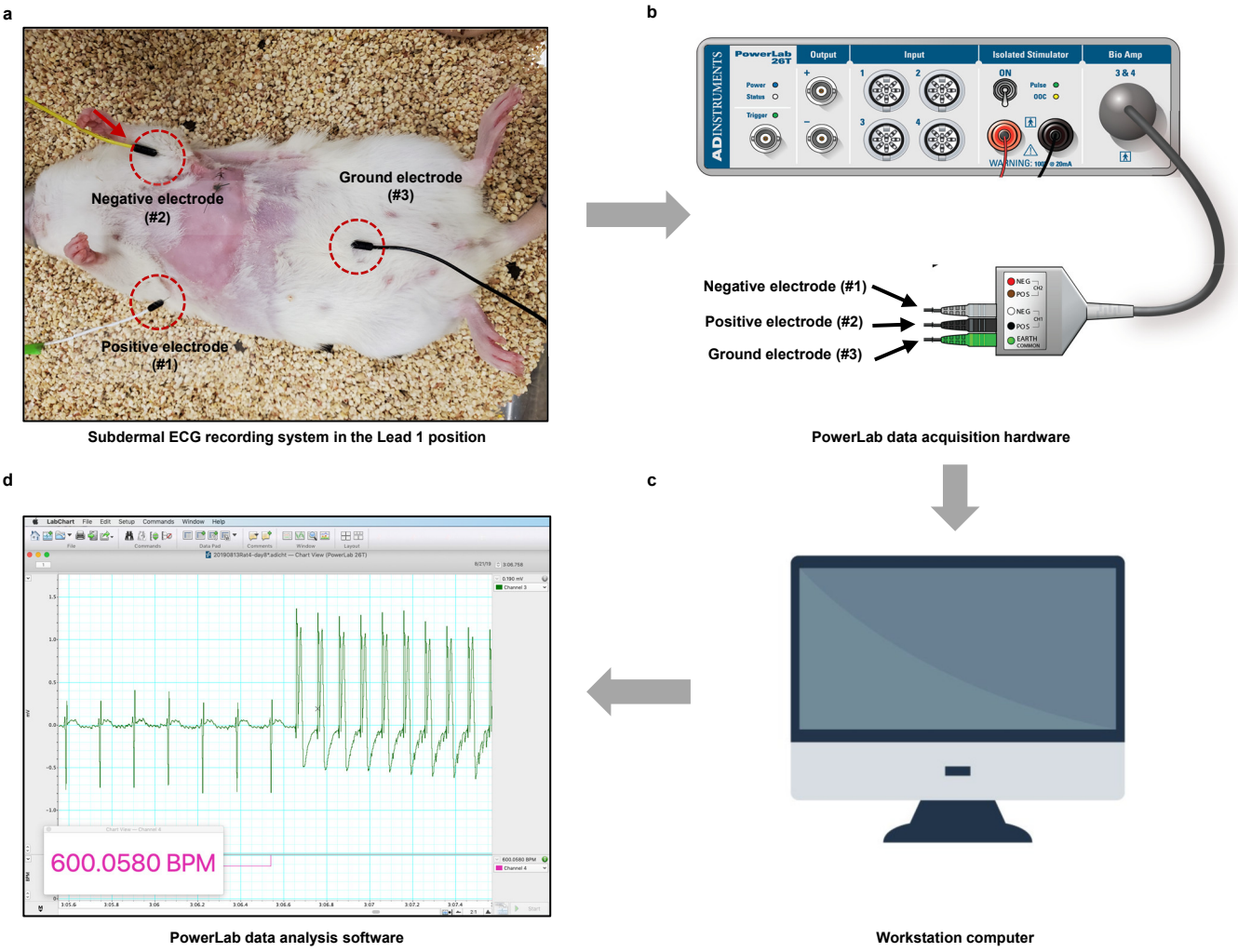

Supplementary Fig. 27 | Commercially available external subdermal ECG acquisition system. a, Subdermal ECG needle electrodes are connected in the Lead I position (positive electrode on right arm, negative electrode on left arm, and ground electrode on the leg). **b,** ECG signal is directly filtered using a Mains filter and a low pass 2 kHz filter. **c, d,** Filtered ECG signals appear in the LabChart data acquisition software (**d**) on a workstation computer (**c**).

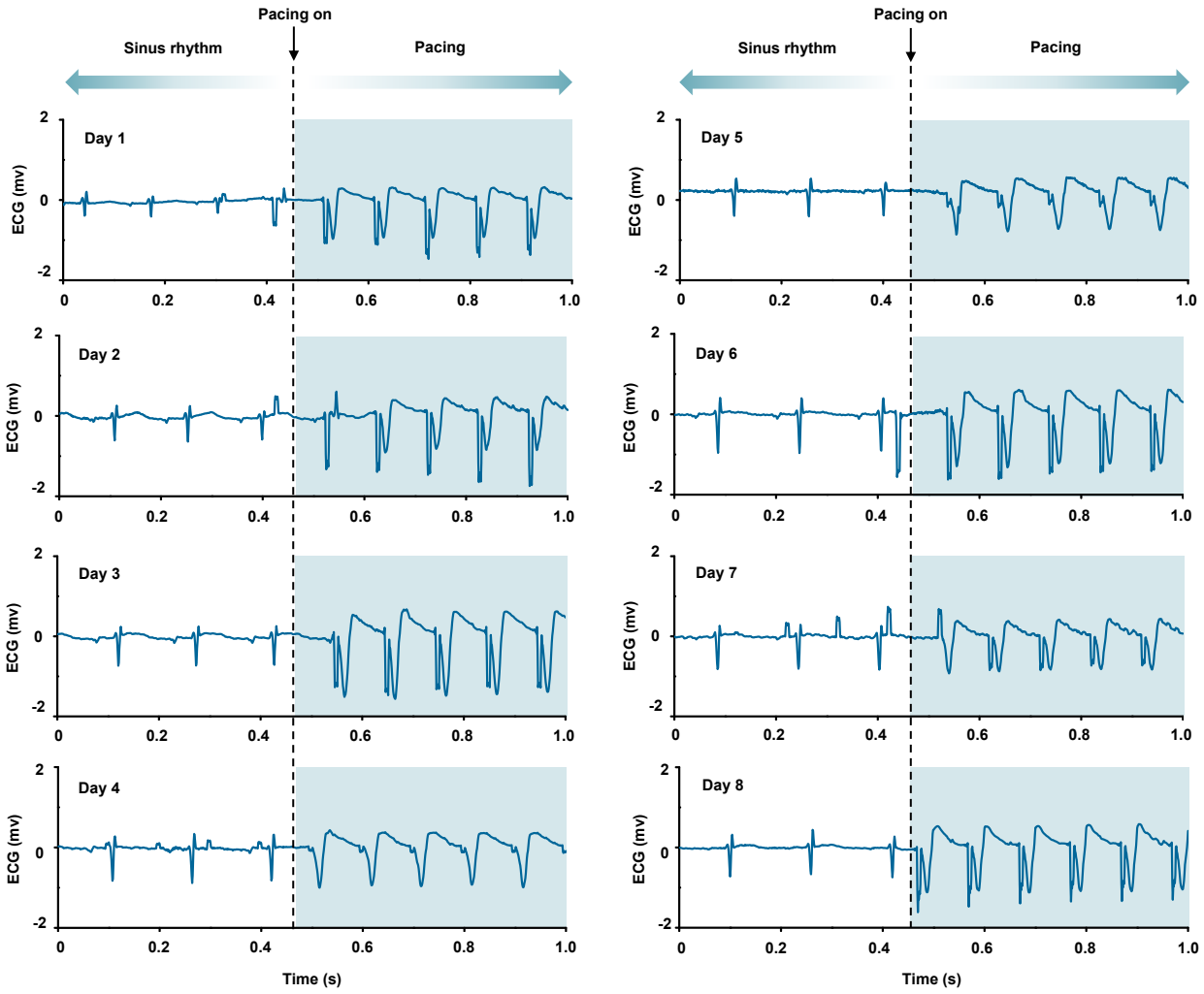

Supplementary Fig. 28 | Representative ECG curves as function of time. ECG traces are obtained by daily ventricular pacing following pacemaker implantation surgery, to assess the functional lifetime of the cardiac pacemakers. BTIM-encapsulated pacemakers provide pacing for up to 8 days after surgery.

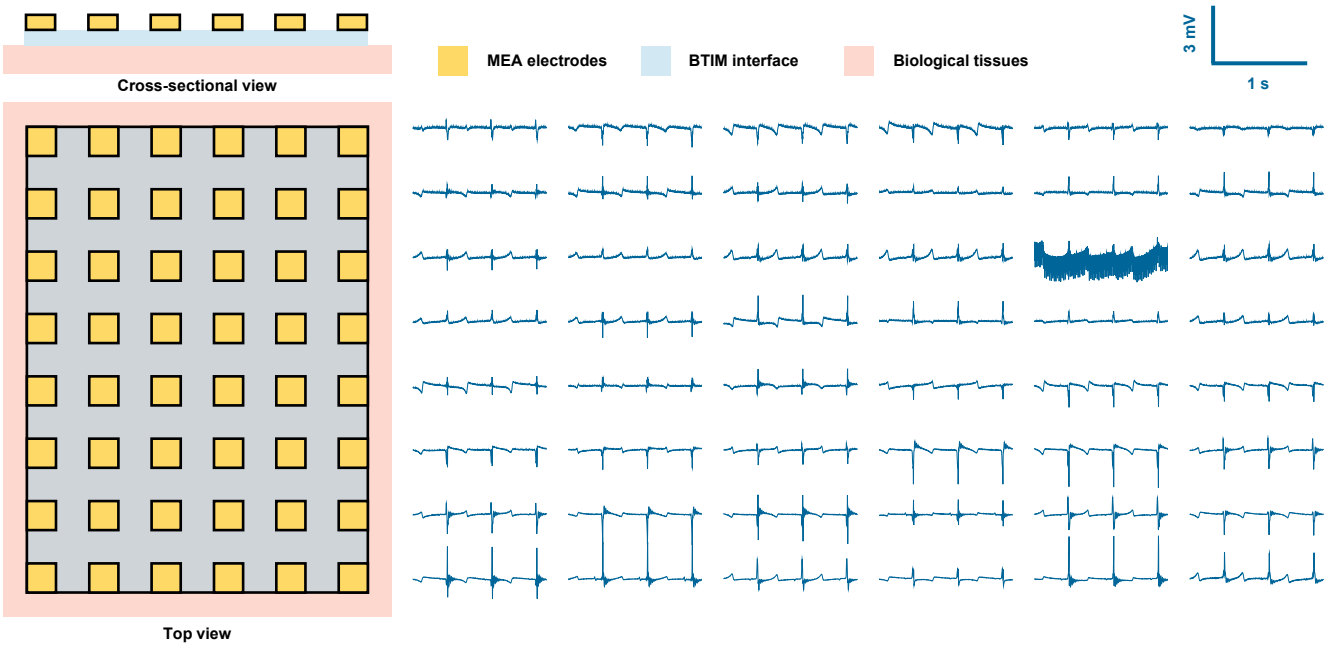

Supplementary Fig. 29 | Electrogram traces measured from each electrode in MEA on a rabbit heart. 48 simultaneous electrograms recorded by a BTIM-interfaced MEA from a Langendorff-perfused rabbit heart for electrical cardiac mapping. Differences in electrode morphology prove that the device functionally operates as expected of a multielectrode system rather than as a single electrode equivalent.

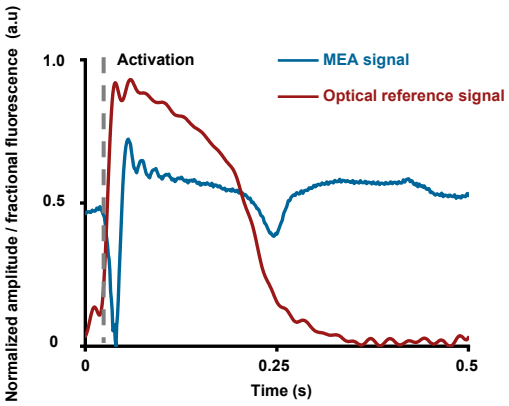

Supplementary Fig. 30 | Simultaneous recordings of electrograms from MEA and reference. The minimum slope on the electrogram, that is, the activation time, corresponds to the maximum upstroke on the optical action potentials (OAP; reference), indicating a consistent relationship between the electrical and optical signals.

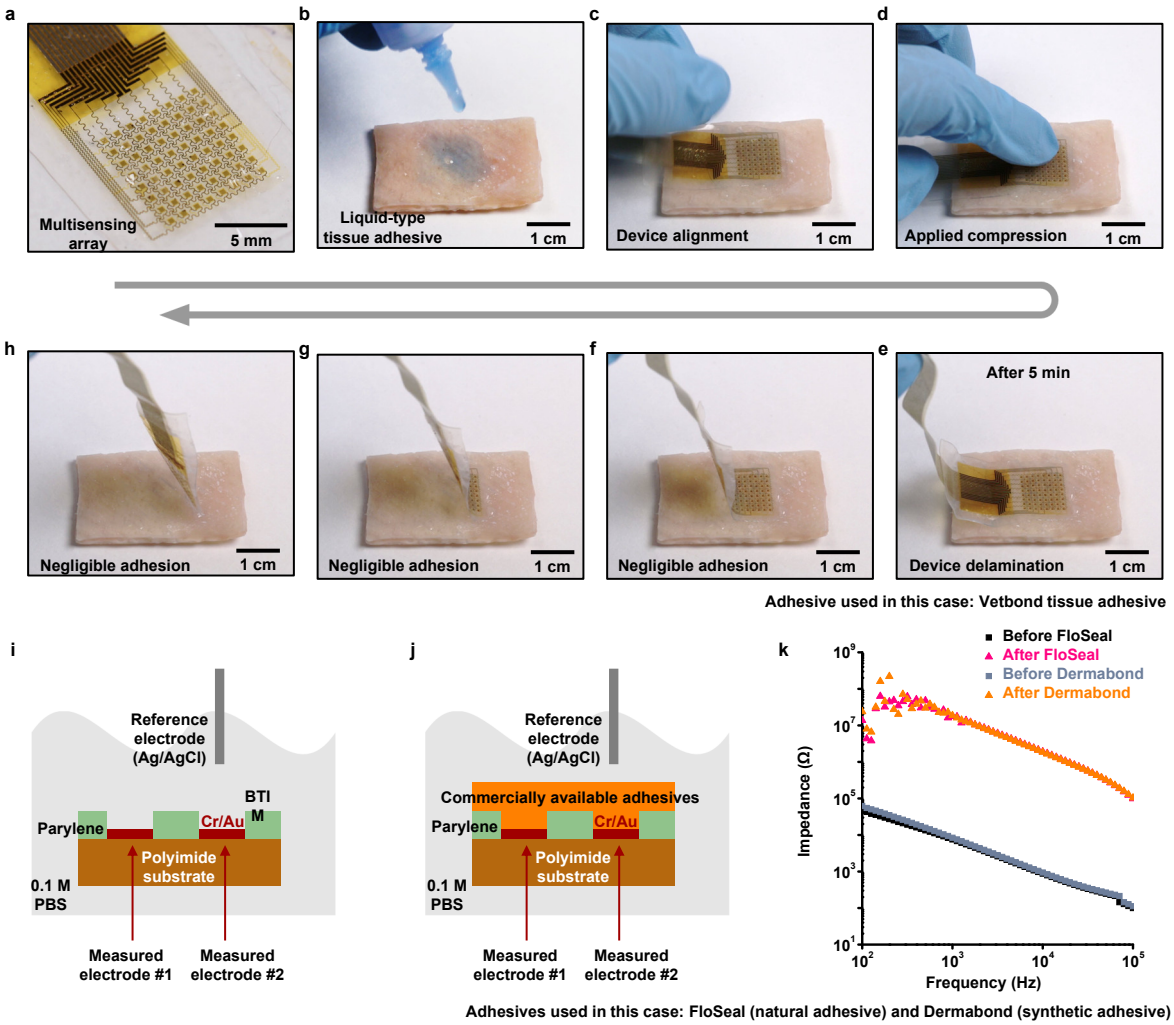

Supplementary Fig. 31 | Ineffectiveness of commercially available tissue adhesives. a-h, Inadequate as adhesives to wet surfaces. These adhesives have low viscosities, and they offer insufficient adhesion strength for practical applications. **i-k,** Inadequate as electrical interfaces. These adhesives lack electrical conductivity and therefore prevent electrical exchange for bioelectronics interfaces.

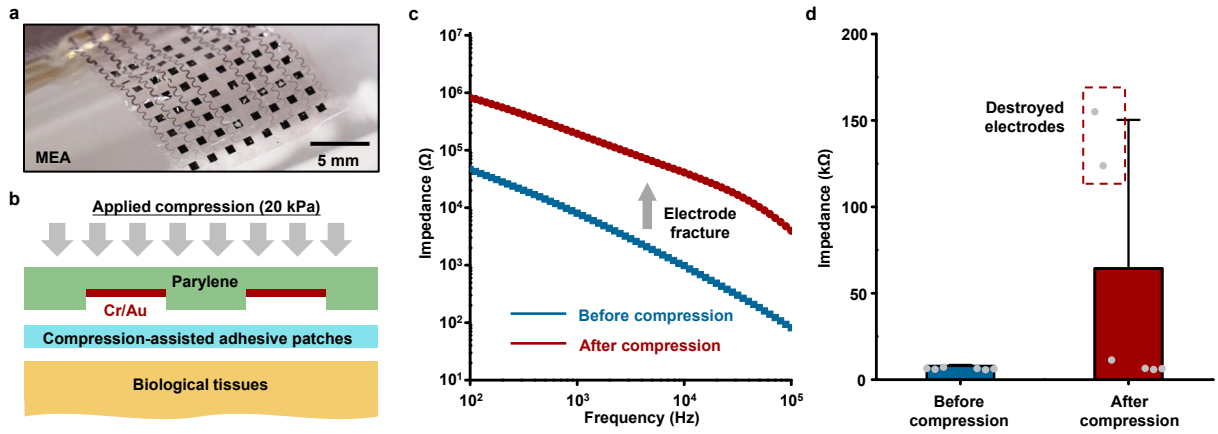

Supplementary Fig. 32 | Fracture of a bioelectronic device induced by compression-assisted adhesive patches. a, Image of an MEA device (parylene/Cr/Au/parylene: 4 μm/30 nm/300 nm/4 μm). **b,** Schematic illustration of pressure (pressure: 20 kPa; duration: 1 min) applied to bond the MEA to biological tissue with a compression-assisted adhesive patch. **c,** Representative impedance spectra of an MEA electrode before (blue) and after (red) compression in 0.1 M PBS at room temperature, suggesting that the impedance increases by two orders of magnitude due to the electrode fracture. **d,** Statistical summary of impedance values before and after compression, revealing that 2 out of 6 electrodes fracture during the compression, at 1 kHz in 0.1 M PBS at room temperature. $n = 6$ independent samples in **d**. Values in **d** represent the mean ± standard deviation.

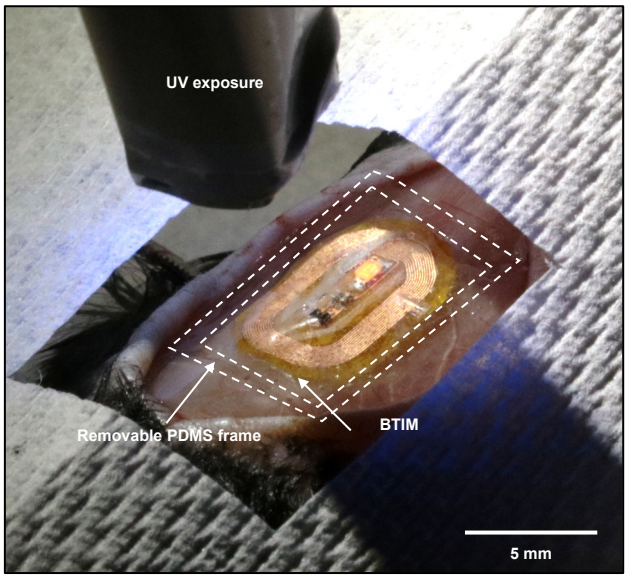

Supplementary Fig. 33 | Spatially confined, uniform patterns of BTIM formed by using frame structures. The PDMS frame, which is removable and biocompatible, (thickness: 500 μm) defines the pattern of liquid cast BTIM for dorsal-subcutaneous wireless optoelectronic devices.

Supplementary Videos

Supplementary Video 1 | Optoelectronic device remains in the bonded location and exhibits stable operation during natural movements of animals. The device can be wirelessly activated to emit red light (peak wavelength: 630 nm), designed for its relevance in tumor irradiation.

Supplementary Video 2 | BTIM firmly secures an optoelectronic device to the dorsal subcutaneous area throughout 2 months post-surgery. The BTIM severs as an encapsulating coating in this situation.

Supplementary Video 3 | Optoelectronic device encapsulated by the BTIM remains functional throughout 2 months post-surgery.

Supplementary Video 4 | Instability of the device coil on the mouse skull without the BTIM.

Supplementary Video 5 | Stability of the device coil on the mouse skull with the BTIM encapsulating coating.

Supplementary Video 6 | Battery-free devices designed for optogenetics remain functional throughout 2 weeks post-surgery. The BTIM serves as an encapsulating coating in this situation.

Supplementary Video 7 | Robust adhesion of the BTIM to a mouse cerebrum.

Supplementary Video 8 | Adhesive conduit supports and protects an interconnect/cable under compression *in vivo*.

Supplementary Video 9 | BTIM in the encapsulation strategy establishes conformal contact between electrodes of wireless cardiac pacemakers and the myocardium *in vivo*.

Supplementary Video 10 | *In vivo* characterization of adhesion between electrodes and the epicardium. The heart can be dragged out of the chest due to the robust adhesion provided by the BTIM.

Supplementary Video 11 | Characterization of adhesion between electrodes and the epicardium on day 10 post-surgery. The robust adhesion remains *in vivo* after 10 days post-surgery.

Supplementary Video 12 | *In vivo* representative ECG traces during rapid ventricular pacing at ~ 1000 bpm.

Supplementary Video 13 | Accurate mapping of ventricular fibrillation on a Langendorff-perfused rabbit heart. The BTIM serves as the interfacial layer in this situation to bridge the MEA and the myocardium.

References

1. Sierra, D. H. Fibrin sealant adhesive systems: a review of their chemistry, material properties and clinical applications. *Journal of Biomaterials Applications* **7**, 309–352 (1993).
2. Lee, Y. J. *et al.* Biocompatibility of a novel cyanoacrylate based tissue adhesive: cytotoxicity and biochemical property evaluation. *PLoS ONE* **8**, e79761 (2013).
3. Vakalopoulos, K. A. *et al.* Mechanical strength and rheological properties of tissue adhesives with regard to colorectal anastomosis. *Annals of Surgery* **261**, 323–331 (2015).
4. Dastjerdi, A. K., Pagano, M., Kaartinen, M. T., McKee, M. D. & Barthelat, F. Cohesive behavior of soft biological adhesives: experiments and modeling. *Acta Biomaterialia* **8**, 3349–3359 (2012).
5. Liang, S. *et al.* Paintable and rapidly bondable conductive hydrogels as therapeutic cardiac patches. *Advanced Materials* **30**, 1704235 (2018).
6. Yuk, H. *et al.* Dry double-sided tape for adhesion of wet tissues and devices. *Nature* **575**, 169–174 (2019).
7. Li, J. *et al.* Tough adhesives for diverse wet surfaces. *Science* **357**, 378–381 (2017).
8. Han, M. *et al.* Catheter-integrated soft multilayer electronic arrays for multiplexed sensing and actuation during cardiac surgery. *Nature Biomedical Engineering* **4**, 997–1009 (2020).
9. Park, Y. *et al.* Three-dimensional, multifunctional neural interfaces for cortical spheroids and engineered assembloids. *Science Advances* **7**, eabf9153 (2021).
10. Xu, L. *et al.* 3D multifunctional integumentary membranes for spatiotemporal cardiac measurements and stimulation across the entire epicardium. *Nature Communications* **5**, 3329 (2014).
11. Kim, D.-H. *et al.* Materials for multifunctional balloon catheters with capabilities in cardiac electrophysiological mapping and ablation therapy. *Nature Materials* **10**, 316–323 (2011).
12. Markov, A. *et al.* Controlled engineering of oxide surfaces for bioelectronics applications using organic mixed monolayers. *ACS Applied Materials & Interfaces* **9**, 29265–29272 (2017).
13. Xu, C., Lee, W., Dai, G. & Hong, Y. Highly elastic biodegradable single-network hydrogel for cell printing. *ACS Applied Materials & Interfaces* **10**, 9969–9979 (2018).
14. Yanniotis, S., Skaltsi, S. & Karaburnioti, S. Effect of moisture content on the viscosity of honey at different temperatures. *Journal of Food Engineering* **72**, 372–377 (2006).
15. Al-Shamkhani, A. & Duncan, R. Radioiodination of alginate via covalently-bound tyrosinamide allows monitoring of its fate *in vivo*. *Journal of Bioactive and Compatible Polymers* **10**, 4–13 (1995).
16. Carnicer-Lombarte, Alejandro, Damiano G. Barone, Ivan B. Dimov, Russel S. Hamilton, Malwina Prater, Xiaohui Zhao, Alexandra L. Rutz, George G. Malliaras, Stephanie P. Lacour, Clare E. Bryant, James W. Fawceet, K. F. Mechanical matching of implant to host minimises foreign body reaction. *bioRxiv* 829648 (2019) doi:10.1101/829648.
17. Yang, Q. *et al.* Materials, mechanics designs, and bioresorbable multisensor platforms for pressure monitoring in the intracranial space. *Advanced Functional Materials* **30**, 1910718 (2020).
18. Song, E., Li, J., Won, S. M., Bai, W. & Rogers, J. A. Materials for flexible bioelectronic systems as chronic neural interfaces. *Nature Materials* **19**, 590–603 (2020).

19. Phan, H.-P. *et al.* Long-lived, transferred crystalline silicon carbide nanomembranes for implantable flexible electronics. *ACS Nano* **13**, 11572–11581 (2019).
20. Mond, H. G., Helland, J. R., Stokes, K., Bornzin, G. A. & McVenes, R. The electrode-tissue interface: the revolutionary role of steroid-elution. *Pacing and Clinical Electrophysiology* **37**, 1232–1249 (2014).
21. FitzGerald, J. J. Suppression of scarring in peripheral nerve implants by drug elution. *Journal of Neural Engineering* **13**, 026006 (2016).